Monthly Notices
of the
ROYAL ASTRONOMICAL SOCIETY

MNRAS **473,** 1512–1536 (2018)
Advance Access publication 2017 September 22

doi:10.1093/mnras/stx2407

The Arcminute Microkelvin Imager catalogue of gamma-ray burst afterglows at 15.7 GHz

G. E. Anderson,[1,2★] T. D. Staley,[1] A. J. van der Horst,[3,4] R. P. Fender,[1] A. Rowlinson,[5,6] K. P. Mooley,[1] J. W. Broderick,[1,5] R. A. M. J. Wijers,[6] C. Rumsey[7] and D. J. Titterington[7]

[1]*Department of Physics, Astrophysics, University of Oxford, Denys Wilkinson Building, Oxford OX1 3RH, UK*
[2]*International Centre for Radio Astronomy Research, Curtin University, GPO Box U1987, Perth, WA 6845, Australia*
[3]*Department of Physics, The George Washington University, 725 21st Street NW, Washington, DC 20052, USA*
[4]*Astronomy, Physics, and Statistics Institute of Sciences (APSIS), The George Washington University, Washington, DC 20052, USA*
[5]*ASTRON, the Netherlands Institute for Radio Astronomy, Postbus 2, NL-7990 AA Dwingeloo, the Netherlands*
[6]*Anton Pannekoek Institute for Astronomy, University of Amsterdam, Postbus 94249, NL-1090 GE Amsterdam, the Netherlands*
[7]*Astrophysics Group, Cavendish Laboratory, 19 J J Thomson Avenue, Cambridge CB3 0HE, UK*

Accepted 2017 September 14. Received 2017 August 29; in original form 2017 July 2

ABSTRACT

We present the Arcminute Microkelvin Imager (AMI) Large Array catalogue of 139 gamma-ray bursts (GRBs). AMI observes at a central frequency of 15.7 GHz and is equipped with a fully automated rapid-response mode, which enables the telescope to respond to high-energy transients detected by *Swift*. On receiving a transient alert, AMI can be on-target within 2 min, scheduling later start times if the source is below the horizon. Further AMI observations are manually scheduled for several days following the trigger. The AMI GRB programme probes the early-time (<1 d) radio properties of GRBs, and has obtained some of the earliest radio detections (GRB 130427A at 0.36 and GRB 130907A at 0.51 d post-burst). As all *Swift* GRBs visible to AMI are observed, this catalogue provides the first representative sample of GRB radio properties, unbiased by multiwavelength selection criteria. We report the detection of six GRB radio afterglows that were not previously detected by other radio telescopes, increasing the rate of radio detections by 50 per cent over an 18-month period. The AMI catalogue implies a *Swift* GRB radio detection rate of $\gtrsim$15 per cent, down to $\sim$0.2 mJy beam^{-1}. However, scaling this by the fraction of GRBs AMI would have detected in the Chandra & Frail sample (all radio-observed GRBs between 1997 and 2011), it is possible $\sim$44–56 per cent of *Swift* GRBs are radio bright, down to $\sim$0.1–0.15 mJy beam^{-1}. This increase from the Chandra & Frail rate ($\sim$30 per cent) is likely due to the AMI rapid-response mode, which allows observations to begin while the reverse-shock is contributing to the radio afterglow.

Key words: gamma-ray burst: general – radio continuum: transients.

1 INTRODUCTION

The first detection of a gamma-ray burst (GRB) at radio wavelengths (GRB 970508; Galama et al. 1998; Frail, Waxman & Kulkarni 2000) brought about a new era of transient astrophysics that has led to over 20 yr of discovery (Frail et al. 2003; Chandra & Frail 2012; de Ugarte Postigo et al. 2012). With the launch of *Swift* in 2004, the improved ability to localize GRBs to within 4 armin (Krimm et al. 2013) using the Burst Alert Telescope (BAT; Barthelmy et al. 2005), with more precise localization being provided by the *Swift* X-ray Telescope (XRT; Burrows et al. 2000) and the *Swift* Ultraviolet/Optical Telescope (UVOT; Roming et al. 2005), has allowed for the rapid identification of hundreds of multiwavelength counterparts. However, despite such a rich data set, a conclusive picture of the radio afterglow properties of GRBs is yet to emerge.

The study of GRBs at radio wavelengths is important because the radio domain provides a unique probe of the associated jet and its interaction with the surrounding circumstellar environment. Such observations, particularly when the jet has decelerated to non-relativistic speeds, also allow us to investigate the total energy budget from these events (Frail et al. 2001). The standard model for GRBs is the internal–external shock scenario (Rees & Meszaros 1992; Piran 1999). This model suggests that along with

★ E-mail: gemma.anderson@curtin.edu.au

the forward-shock created by the blast wave at the front of the relativistic jet propagating into the circumstellar medium (observed as the classical afterglow), there is a reverse-shock that propagates back into the relativistic ejecta causing a much faster flash of emission (Sari & Piran 1999). The transient radio emission associated with the reverse-shock occurs within a few hours to a few days post-burst (Kulkarni et al. 1999), and therefore requires a rapid observing response in order to be detected.

In an attempt to understand the radio properties of GRBs, Chandra & Frail (2012) conducted a complete investigation of all historical events observed in the radio domain. These included both of the main GRB populations (Kouveliotou et al. 1993): long-duration GRBs (likely produced by massive stellar collapse where the gamma-ray emission lasts for more than 2 s; Woosley 1993; Kulkarni et al. 1998; Woosley & Bloom 2006) and short-duration GRBs (likely caused by the coalescence of two neutron stars or a neutron star and black hole, which lasts for less than 2 s; Lattimer & Schramm 1976; Eichler et al. 1989; Narayan, Paczynski & Piran 1992). Only 30 per cent of their sample had a detectable radio afterglow, with the radio emission peaking within a very narrow flux range. This led them to conclude that the low percentage of detections was likely due to the sensitivity of radio telescopes rather than there being two distinct GRB populations: radio-bright and radio-faint. Ghirlanda et al. (2013) and Burlon et al. (2015) then conducted simulations to demonstrate that potentially all *Swift* GRBs will be detectable at radio frequencies with phase 1 of the Square Kilometre Array (SKA), specifically SKA1-MID in Band 5 ($\sim$9 GHz)[1] between 2 and 10 d post-burst, as well as with the recently upgraded Karl G. Jansky Very Large Array (VLA)[2] and MeerKAT (the South African SKA precursor telescope; Jonas 2009). In fact, SKA1-MID will be so sensitive it could detect the radio counterparts from GRBs with gamma-ray emission up to five times fainter than those currently detected with *Swift*-BAT (note that these simulations do not account for radio emission produced by the reverse-shock, only considering contributions from the forward-shock; Burlon et al. 2015). However, a study conducted by Hancock, Gaensler & Murphy (2013), which involved visibility stacking of VLA GRB radio observations, suggested the low radio detection rate may be due to there being separate radio-bright and radio-faint GRB populations, and that $\leq$70 per cent are likely to be truly radio bright.

While Chandra & Frail (2012) provide a very comprehensive study of all radio-observed GRBs up until 2011 January, their sample may not be representative of the entire GRB population. Due to the limited number of radio telescopes, the amount of available radio observing time is at a premium, so choosing the best GRBs to follow-up is often based on existing knowledge of the event to ensure the greatest chance of a radio afterglow detection. Such criteria usually include a bright optical or X-ray counterpart, its close proximity to the Milky Way, or the suspicion of the GRB being an optically dark burst (van der Horst et al. 2009, 2015). Additionally, while a vast quantity of early-time (within minutes of the burst) optical and X-ray data on GRBs have been collected (see Gehrels, Ramirez-Ruiz & Fox 2009, and references therein), once again, the rarity of radio telescopes has led to fewer experiments designed to obtain similar early-time observations at radio wavelengths. We clearly require a programme capable of targeting the early-time radio properties of GRBs (<1 d post-burst), which are specifically sensitive to the reverse-shock contributions to the radio afterglow. The programme design would also need to provide a radio detection rate more representative of the GRB sample (i.e. not informed by multiwavelength properties).

In order to probe the early-time radio properties of GRBs, one solution is to implement a rapid-response observing system, which enables telescopes to trigger on transient alerts, such as *Swift*-detected GRBs. Such a system automatically repoints the telescope, allowing it to begin observing the transient within minutes of its detection. While uncommon, radio telescopes capable of responding to external triggers have existed for at least 20 yr. The first triggering programmes were specifically designed to probe for prompt, coherent radio emission associated with GRBs, with time-scales on the order of milliseconds. For example, the Cambridge Low Frequency Synthesis Telescope performed triggered observations of Burst And Transient Source Experiment (BATSE) GRBs, placing limits on prompt emission on the order of 10's Jy at 151 MHz (Green et al. 1995; Dessenne et al. 1996). In fact, with the discovery of fast radio bursts (FRBs; Lorimer et al. 2007), prompt radio emission associated with GRBs became one of the top progenitor candidates. Bannister et al. (2012) used a 12 m radio dish at 1.4 GHz to trigger on nine *Swift* GRBs, possibly detecting a single, highly dispersed short duration radio pulse at 6 times the root-mean-square (rms) noise (σ_s) from two GRBs. While work by Zhang (2014) supports a possible link between GRBs and FRBs (particularly short GRBs), triggered observations performed by Palaniswamy et al. (2014) on five *Swift* GRBs using a 26 m radio dish at 2.3 GHz, failed to detect prompt radio emission above $6\sigma_s$, discouraging an association. The Murchison Widefield Array (MWA; Tingay et al. 2013) also triggers on *Swift* GRBs, and a recent search for prompt radio emission associated with the short GRB 150424A placed 3 Jy flux limits on 4 s, 2 min and 30 min time-scales between 80 and 133 MHz (Kaplan et al. 2015). In each case, these experiments were conducted at low frequencies ($\leq$2.3 GHz) with the specific task of searching for coherent radio emission associated with GRBs. None of these programmes probed for early-time incoherent, synchrotron emission signatures from the forward- or reverse-shock afterglows, which are likely to be bright and evolving on daily time-scales at higher radio frequencies ($\gtrsim$5 GHz).

Clearly there is a need for a longer running radio programme capable of performing rapid-response and long-term monitoring of GRBs to probe associated incoherent radio emission. Over the last 5 yr, we have been running a robotised follow-up programme that automatically triggers the Large Array (LA) interferometer of the Arcminute Microkelvin Imager (AMI; Zwart et al. 2008) on *Swift*-BAT-detected GRBs. This programme is called the AMI-LA Rapid-Response Mode (ALARRM), which is currently the longest running GRB rapid-response follow-up project in the radio domain (Staley et al. 2013). Following a *Swift* trigger, AMI-LA (henceforth referred to as AMI) is capable of being on-target and beginning observations within 2 min post-burst. This programme is therefore capable of statistically constraining the radio properties of GRBs within the first few hours to day post-burst, making it sensitive to radio reverse-shock emission. Continued AMI monitoring is then manually scheduled throughout the following weeks and months, allowing us to obtain a global view of the radio properties of both long and short *Swift*-detected GRBs from a representative sample that have not been informed by multiwavelength observations.

Early AMI-ALARRM results include observations of GRB 130427A, obtaining one of the earliest published radio detections of a long GRB at 0.36 d post-burst, allowing us to follow the rise and decline of the reverse-shock flare in the radio band (Anderson et al. 2014e). Since 2014 May, the ALARRM programme has

[1] See SKA baseline documents http://skatelescope.org/key-documents/
[2] https://science.nrao.edu/facilities/vla

been expanded to also trigger on non-GRB *Swift* transients. Consequently, AMI triggering on the gamma-ray superflare from the rapidly rotating M-dwarf DG CVn, detecting the associated giant radio flare, which represents one of the earliest radio transient detections resulting from a high-energy trigger (Fender et al. 2015). Using the ALARRM mode, AMI was also the first radio telescope to begin observing V404 Cyg just 2 h after the *Swift* detection of its 2015 June 15 outburst, following 26 yr of quiescence (Mooley et al. 2015).

In this paper, we present the AMI GRB catalogue from the first 3 yr of ALARRM triggering and AMI follow-up. This catalogue includes 871 radio flux densities and limits at 15.7 GHz for 139 GRBs, 132 of which were detected by *Swift*-BAT, with comprehensive and systematic temporal coverage spanning <2 min up to several months post-burst. A description of the AMI/ALARRM observing strategy, data reduction and GRB radio counterpart identification can be found in Section 2 with the complete AMI GRB catalogue presented in Section 3. In Section 4, we discuss individual GRBs that were detected with AMI. These include new radio GRBs, which were first detected in the radio band by AMI, and radio-detected GRBs (initially identified by other radio telescopes). We also briefly describe those GRBs for which we have possible AMI detections and those that appear coincident with a steady radio source. Known radio-detected GRBs that were not detected with AMI are also examined. In Section 5, we discuss the overall statistical properties and implications of the AMI GRB catalogue, which represent the first systematic radio survey of *Swift*-detected GRBs. This includes discussions on the early-time radio properties of GRBs (<1 h post-burst), the radio GRB detection rate, and the radio brightness temperatures, minimum Lorentz factors and luminosities. Our summary and conclusions can be found in Section 6.

2 OBSERVING STRATEGY AND DATA ANALYSIS

2.1 AMI strategy and observations

The radio observations of GRBs presented in this paper were obtained using AMI, which is a radio interferometer consisting of eight 12.8 m diameter dishes with baselines between 18 and 110 m. As all the observations were conducted prior to 2015 June, the effective frequency range was 13.9–17.5 GHz using channels 3–7, each with a bandwidth of 0.72 GHz, with channels 1, 2 and 8 being disregarded due to their susceptibility to radio frequency interference (RFI). AMI measures a single polarization ($I + Q$) and has a flux rms noise sensitivity of 3.3 mJy $s^{-1/2}$ for five frequency channels. At the central operating frequency of 15.7 GHz, AMI has a primary beam of 5.5 arcmin and a ≈30 arcsec resolution (Zwart et al. 2008). During each AMI observation, a bright unresolved source within a few degrees of the target of interest is visited for 1 min in every 11 min to provide phase and amplitude calibration (for further details on the absolute flux calibration of AMI, see Franzen et al. 2011).

The first stage of the ALARRM observing strategy involves AMI receiving a GRB alert from *Swift*-BAT, which triggers a fully automated AMI observation of the event, now with response times within 2 min post-burst. The *Swift*-BAT trigger is broadcast via a VOEvent, which is a standard format for distributing information regarding astronomical transient alerts such as the source position, classification and fluxes.[3] The VOEvent alerts are then parsed by the '4 Pi Sky' VOEvent broker (Staley & Fender 2016), which triggers a rapid-response AMI observation of the transient. If the GRB is above the declination cut-off but below the horizon, the software will automatically update the AMI schedule to begin observations when the source has risen above the horizon. As the *Swift*-BAT position is only accurate to within 1–4 arcmin (Gehrels et al. 2004), it is likely that the true GRB position will be off-centre, but still contained within the AMI primary beam. Follow-up AMI observations designed to detect late-time radio emission are then manually scheduled using updated positions supplied by *Swift*-XRT or *Swift*-UVOT.

The early results of the ALARRM programme were first described by Staley et al. (2013). Of the 11 GRBs reported, only GRB 120326A was detected by AMI, with all non-detections listed as upper limits. At this stage of the programme, AMI triggered on all *Swift*-BAT-detected GRBs with a declination $\delta > -10^{\circ}$. If the GRB was above the horizon, then AMI was capable of being on-target within 5 min post-burst. The resulting triggered observation and subsequent manually scheduled observations were 1 h in duration and followed a logarithmic follow-up schedule (for specific details on the automation of the AMI telescope and the original trigger policy, please see Staley et al. 2013).

By the end of 1 yr of operation the only radio counterparts detected were from GRB 120326A and GRB 130427A, with only one spectacular early detection coming from the latter (Anderson et al. 2014e). The average sensitivity of these observations were 0.1 mJy $beam^{-1}$, with progressively worse rms noise levels for lower declinations. The ALARRM triggered observations also tended to have worse rms noise levels as these often occurred closer to the horizon and therefore suffered more severely from terrestrial RFI. With the detection of only 2 out of 68 AMI observed GRBs, 9 of which were detected in the radio band by other instruments, we decided to adjust the ALARRM strategy.

The updated ALARRM strategy, which was implemented in 2013 August and ran until the old correlator was shut down in mid-2015, was aimed at obtaining a larger proportion of GRB radio counterpart detections with a smaller number of triggered and manually scheduled observations. ALARRM observations were restricted to all *Swift* triggers that had a declination $\delta \geq 15^{\circ}$ to decrease the amount of RFI due to low elevation angles. The *Swift* triggered AMI observations were extended to 2 h in order to obtain a more sensitive observation, but short enough to not significantly disrupt the calibrator observing schedule, which is crucial for telescope operations. Additional software changes were implemented to decrease the reaction time of the telescope, allowing us to be observing the target <2 min post-burst.

The duration of the manually scheduled follow-up observations were also increased to improve the likelihood of a radio detection. The recent investigation of the entire sample of radio-detected GRBs before 2011 April by Chandra & Frail (2012) demonstrated that the majority of GRBs detected in the radio band at 8.5 GHz had a peak flux between 0.1 and 0.2 mJy $beam^{-1}$ at 5–10 d post-burst (see fig. 4 of Chandra & Frail 2012). A 4 h AMI observation is therefore required to reach an rms noise of ∼0.03–0.04 mJy $beam^{-1}$ that will allow the reliable detection of >0.1–0.2 mJy $beam^{-1}$ sources. However, it is worth noting that since GRB relativistic blast waves generate synchrotron radiation as they expand into the circumstellar (wind generated) medium (Granot & Sari 2002), we expect the forward-shock of the afterglow to peak more brightly at 15.7 GHz and at earlier times than the peaks recorded by Chandra & Frail (2012). We therefore require a higher monitoring cadence at early times (within 5 d post-burst) to detect similar radio peaks. As the

[3] http://wiki.ivoa.net/bin/view/IVOA/IvoaVOEvent

range of radio peaks observed by Chandra & Frail (2012) will be brighter at 15.7 GHz, the rms achieved by a 4 h AMI observation will be sufficient for detecting events similar to those seen in their sample. The follow-up observations are manually scheduled to occur near transit approximately 24 h, 3, 7, and 10 d post-burst, with this temporal spacing designed to catch the peak of the forward- or reverse-shock at 15.7 GHz at a range of redshifts ($z \lesssim 5$; e.g. see figs 22 and 23 of Chandra & Frail 2012). In the event that a GRB radio counterpart was detected, the AMI observing cadence was increased to a 4 h observation every 1 or 2 d. As part of the AMI GRB observing programme, we also obtained manually scheduled observations of GRBs that were detected with the *Fermi* Large Area Telescope (LAT; Atwood et al. 2009), the *Fermi* Gamma-ray Burst Monitor (GBM; Meegan et al. 2009) and the *International Gamma-Ray Astrophysics Laboratory* (*INTEGRAL*; Winkler et al. 2003), whose positions had been more precisely localized through the identification of X-ray and/or optical counterparts, usually by the *Swift*-XRT, *Swift*-UVOT, or one of the ground-based GRB follow-up programmes.

2.2 Pipeline reduction and analysis

The development of fully automated reduction pipelines, capable of calibrating, imaging and analysing radio data are crucial for the preparation of the SKA (and its pathfinders) in order to minimize the human effort required for processing the projected vast data volumes. With this in mind, we constructed a pipeline specifically designed to deal with multi-epoch radio observations of transients that was built upon mature radio astronomy software packages using PYTHON as the interface. The resulting software package AMISURVEY (Staley & Anderson 2015a) utilizes dedicated PYTHON libraries that were built to allow use of the AMI-REDUCE software suite (Dickinson et al. 2004) and the Common Astronomy Software Applications package (CASA; Jaeger 2008).

The calibration stage of AMISURVEY calls on the PYTHON library DRIVE-AMI (first introduced by Staley et al. 2013) built upon AMI-REDUCE. AMI-REDUCE is designed to take the raw AMI data set and automatically flag for interference, shadowing, and hardware errors, apply phase and amplitude calibration, and Fourier transform the data. These processes are automated by a AMI-REDUCE script that also searches for, and applies, adaptive amplitude flagging to known sources of interference. The AMI-REDUCE script applied to the AMI GRB observations used a more relaxed adaptive flagging than what is usually applied to AMI data as we found that standard amplitude cut-offs potentially attenuated the measured point source fluxes by ∼10 per cent. It is therefore possible that the measured fluxes reported in this catalogue are slightly overestimated due to potentially unflagged interference. AMI-REDUCE then outputs the data as *uv*-FITS files that are suitable for imaging in standard radio analysis software.

The imaging stage of AMISURVEY is conduced using CHIMENEA, which is built upon CASA and is specifically designed to clean and image multi-epoch radio transient observations (Staley & Anderson 2015b,c). CHIMENEA first takes a list of *uv*-FITS files, converts them to CASA measurement sets and concatenates all epochs with the same pointing centre. The CASA CLEAN algorithm is then used to invert, deconvolve and restore the concatenated data, creating a deep image. CHIMENEA then uses source finding algorithms developed for the LOFAR Transient Key Science Project,[4] specifically the LOFAR Transients Pipeline (TRAP; Swinbank et al. 2015) and the Transients Project source extraction & measurement code (PYSE; Carbone et al. 2017). CHIMENEA identifies sources in the deep image down to a flux significance of four times the rms ($4\sigma_s$ level), the positions of which are used to create a clean mask to be applied during future cleaning steps, ensuring model components are only placed at known source locations. Additional clean apertures can also be applied by the user at the location of other sources, such as at the known position of a GRB. The final clean mask is applied to each individual radio epoch, along with the concatenated data, which then undergo an iterative cleaning process. This recleaning action continues down to a predefined flux threshold that is usually three times the rms noise. This iterative cleaning process is necessary as the sidelobes from bright field sources reduce with each clean attempt, lowering the background rms noise and therefore allowing for a deeper clean. The $3\sigma_s$ threshold then prevents overcleaning, which can cause artificial changes in source fluxes and image background noise levels (also known as 'clean bias'). The final cleaned images from both the individual epochs and concatenated data (deep image) are output in FITS format. Note that the final images were not primary beam corrected as this correction severely distorts the Gaussian shape of the point sources in the AMI data. The primary beam correction is applied manually to the measured fluxes and upper limits in the final catalogue.

2.3 Radio counterpart detection and identification

All the individual AMI epochs and deep concatenated images (created by only concatenating those epochs with the same pointing centre) were searched for GRB radio afterglow detections using PYSE. We searched for all sources with a $>4\sigma_s$ flux significance that were within three times the positional uncertainty (σ_p) of the best-known *Swift* position of the GRB (see details below). These sources then became candidate afterglow detections. For those GRBs where no radio counterpart candidate was detected, we used PYSE to perform a forced fit at the best-known *Swift* position, assuming a point source with a size and shape fixed to that of the restoring beam. These algorithms report the position of any detected radio sources, plus the flux and significance of all detections and forced fits, along with the statistical errors (based on Condon et al. 1998).

In order to determine the false source detection rate in our AMI observations at different levels of significance, we ran PYSE on the deep concatenated image of each GRB to obtain a true and deep catalogue of all the radio sources in each field. All those sources with a flux significance $>3\sigma_s$ that were detected in the individual epochs by PYSE within the primary beam, but were not detected in the deep concatenated image of that particular GRB, were considered false detections (further investigations as to whether these sources are transients is beyond the scope of this paper). A radio source in an individual epoch was considered to be the same as a source in the deep concatenated image if the angular distance between them was less than three times the $1\sigma_p$ position error (this excludes all $>3\sigma_s$ detected sources within three times the positional error of the *Swift* GRB position to avoid contamination from a radio counterpart below the detection threshold defined below). After visually inspecting the data and removing all false sources that appeared to be artefacts from nearby bright sources, our analysis found 12 possible false sources with a flux significance between $3 < \sigma_s < 4$, and 6 possible false sources within a flux significance between $4 < \sigma_s < 5$, with none above $5\sigma_s$ in 871 AMI observations. If we assume that these false sources came from random Gaussian noise fluctuations, then we can calculate the probability of a false source to occur at the

[4] http://docs.transientskp.org; https://github.com/transientskp/tkp

position of a GRB in the 871 observations. In most cases, the position error of a GRB is within the AMI-synthesized beam (<30 arcsec), of which ∼100 fill the AMI primary beam. Therefore, in 87 100 samples (100 beams in 871 observations), there is a 0.014 per cent and 0.007 per cent chance of a false source being detected at the position of the GRB with a flux significance between $3 < \sigma_s < 4$ and $\sigma_s > 4$, respectively. Given it is twice as likely for a false source to be detected with a flux significance between $3 < \sigma_s < 4$ than with a flux significance $\sigma_s > 4$, we have chosen to only report radio detections at the position of the GRB with a flux significance of $\sigma_s > 4$.

To identify those GRBs with a candidate radio afterglows, we ran a source matching algorithm designed to pair any AMI-detected radio source with a GRB provided the angular distance between the two positions were within three times the total $1\sigma_p$ position error, which is the *Swift* GRB position error added in quadrature to the radio source position error calculated by PYSE. In some sets of AMI observations, the angular distance between an AMI-detected radio source and GRB was $\leq 3\sigma_p$ at some epochs but $>3\sigma_p$ at others. We therefore define an AMI radio source to be the same source at multiple epochs if their positions agree within $\lesssim 1.5\sigma_p$ of the source position in the deep concatenated image. After a coincident radio source was identified using the above method, the individual AMI observations were visually inspected to ensure it was not diffuse emission or an artefact from a nearby bright source. Once verified, all GRBs with a coincident radio source with a $>4\sigma_s$ significant detection are considered highly likely to be associated.

2.3.1 Radio counterpart selection criteria

Identifying a coincident radio source as a GRB radio afterglow needed to be assessed on a case-by-case basis. Many of the afterglow candidates detected had a $\leq 5\sigma_s$ flux significance and therefore large errors. As a result, it was difficult to test for variability in the radio light curves by deriving a reduced χ^2 to a weighted mean fit (Gaensler & Hunstead 2000). We therefore based our identification of a coincident radio source as a *confirmed* AMI-detected GRB radio afterglow using the following criteria:

(i) The radio source must have been detected in at least two epochs with a flux significance $>4\sigma_s$. This is due to our detecting several false sources in the AMI observations with a significance between $4 < \sigma_s < 5$ (as demonstrated in Section 2.3), which suggests a small chance of a single candidate afterglow detection not being real.

(ii) There must be an early- or late-time non-detection in the AMI observations with rms noise levels that would have detected the radio source at its brightest measured flux with a significance $>5\sigma_s$.

Those GRBs with a coincident radio source that was only detected in one epoch, but are consistent with our second criterion, are considered *possible* AMI-detected GRB radio afterglow.

There were also several GRBs for which no coincident radio source was detected in a single epoch, but one was detected in the deep concatenated image. In such cases, it is possible that the deep concatenated image was sensitive enough to detect the radio afterglow. To investigate this possibility, we divided the individual epochs of the GRB into two even groups, the early epochs and the later epochs, and created two new concatenated images. A radio afterglow would be expected to have different brightnesses in these two concatenated images, thus confirming its variable nature. If the source is detected in both of the concatenated images but with the flux measurements differing by $\geq 4\sigma_s$; or if the source is only detected in one concatenated image with the non-detection in the second concatenated image obeying criterion (ii), then the source will be considered variable and therefore classified as a *confirmed* AMI-detected GRB radio afterglow.

3 THE AMI GRB CATALOGUE

The AMI GRB Catalogue presented in Tables 1 and 2 is the complete list of GRBs observed with AMI as part of the ALARRM programme, from the first triggered observation of GRB 120305A, up until the last observation of GRB 150413A taken on 2015 May 9. Table 1 only reports those GRBs that have a *confirmed* or *possible* radio afterglow detection in the AMI data as defined in Section 2.3.1, all of which are long GRBs. Table 2 lists all other AMI observed GRBs including those reporting coincident/serendipitous steady sources. The full catalogue includes the AMI 15.7 GHz fluxes and upper limits of 139 GRBs from 871 AMI observations, totalling 90.2 d of observing time. Of the 139 GRBs in this catalogue, 132 were detected with *Swift*, which resulted in a triggered rapid-response AMI observation. Of the 132 *Swift*-detection events, 12 were short GRBs. Another five *Fermi*- and two *INTEGRAL*-detected long GRBs were also observed with AMI after their positions were localized through optical and/or X-ray afterglow detections, which were consequently reported on the GRB Coordinates Network (GCN).[5] The *Fermi*- and *INTEGRAL*-discovered GRBs are indicated by the † and ‡ symbols, respectively, in Tables 1 and 2. In Tables 1 and 2, all GRB observations from GRB 130907A and GRB 130813A onwards, respectively, follow the updated ALARRM strategy (see Section 2.1) and are thus used in the detection statistics in Section 5.1.

The AMI GRB Catalogue Tables 1 and 2 include a column indicating whether the GRB has been reported to have radio afterglow, either through the GCN or in the literature. Table 2 also specifies whether the GRB was long or short, where we classify it as a short GRB if its T_{90} (time that the cumulative counts increase from 5 per cent to 95 per cent above background, therefore including 90 per cent of the total GRB counts) is <2 s (Kouveliotou et al. 1993). Note that only long-duration GRBs were detected with AMI. The Telescope column indicates the name of the *Swift* telescope that provided the most localized position of the GRB. This position was used as the reference GRB position when searching for radio afterglows in the AMI data, and is also the position at which a forced fit was applied in the case that a coincident radio source was not detected. The preferred position is from the *Swift*-UVOT, which has a 90 per cent error radius better than 1 arcsec (Roming et al. 2005), followed by the *Swift*-XRT position, with a 90 per cent error radius better than 5 arcsec (Burrows et al. 2008). If neither of these positions were available, which could be due to a faint counterpart or an observing constraint, we tried to find a counterpart position reported on the GCN. If none were reported, we used the position from *Swift*-BAT, which has a 90 per cent error radius between 1 and 4 arcmin.

Tables 1 and 2 then list the basic information of each AMI observation, including the start date of the observations in both Gregorian and MJD formats, the duration of the observation in hours, the time post-burst that the observation commenced in days, and the observational rms noise. The reported peak fluxes for the individual epochs and concatenated deep images (labelled 'concat' in the Tables) are those output by PYSE, which are then primary beam corrected. The

[5] http://gcn.gsfc.nasa.gov/

Table 1. The AMI 15.7 GHz GRB catalogue: GRBs that have been detected or possibly detected with AMI.

GRB[a]	Radio[b] Flag	Telescope[c]	Date[d] (yyyy-mm-dd)	Start[e] (MJD)	Integration[f] (hours)	Days[g] (post-burst)	Peak flux[h] (mJy beam^{-1})	Sig[i]	rms[j] (mJy beam^{-1})
120320A	P	XRT	2012-03-21	56007.09	1.0	0.60	* 0.38 ± 0.09	4.0	0.08
120320A	P	XRT	2012-04-05	56022.06	1.0	15.56	0.15 ± 0.28	9.0	0.09
120320A	P	XRT	Concat				0.15 ± 0.28	9.0	0.06
120326A	R	UVOT	2012-03-26	56012.36	1.0	0.31	− 1.20 ± 8.88	2.6	0.14
120326A	R	UVOT	2012-04-02	56019.21	1.0	7.15	* 0.86 ± 0.1	8.4	0.08
120326A	R	UVOT	2012-04-16	56033.30	1.0	21.25	* 0.37 ± 0.09	4.0	0.08
120326A	R	UVOT	2012-04-28	56045.29	1.0	33.24	0.42 ± 0.14	3.3	0.14
120326A	R	UVOT	Concat				* 0.59 ± 0.08	7.8	0.05

Notes. All GRBs in this table are classed as long GRBs. All GRB observations from GRB 130907A onwards followed the updated ALARRM strategy (see Section 2.1).

[a]GRB discovery flag: †: *Fermi*-discovered GRB; ‡: *INTEGRAL*-discovered GRB.

[b]Radio detection flag: A – new radio GRB discovered with AMI; AC – new radio GRB discovered with AMI that was only detected in the concatenated image; R – radio afterglow first detected with another radio telescope; P – possible new candidate radio GRB discovered with AMI (see Section 4 for further details on these categories).

[c]Best *Swift* telescope position used to search for a radio counterpart: BAT – *Swift* Burst Alert Telescope; XRT – *Swift* X-ray Telescope; UVOT – *Swift* Ultraviolet/Optical Telescope.

[d]Date of the AMI observation in yyyy-mm-dd. Concat – concatenation of all epochs with the same pointing (in the case of GRB 120320A, two observations were taken with different pointings so the concatenated image is the same as the 2012-04-05 epoch).

[e]Start date of the AMI observation in modified julian date (MJD) format.

[f]AMI observation length in hours.

[g]Number of days post-burst since the start of the AMI observation. The response time, in minutes, has also been included in brackets for those AMI observations that began $\leq$0.01 d post-burst.

[h]Peak flux density as reported by PYSE. The '*' symbol indicates those GRBs for which the listed AMI peak flux is the measured flux of a radio source detected above a $4\sigma_s$ significance, coincident with the best-known *Swift* position of the GRB (i.e. within $3\sigma_p$). All other listed fluxes are derived from a forced Gaussian fit at the best-known *Swift* position. The $1\sigma_s$ error bar is the flux error output by PYSE, added in quadrature to the AMI 5 per cent calibration error.

[i]The significance of the AMI flux reported by PYSE, which are measured in units of σ_s above a local rms.

[j]The global rms of the middle quarter of the AMI image.

(The full table is available in the online journal in a machine-readable and PDF form. A portion is shown here for guidance.)

peak fluxes measured from detections of radio sources coincident with GRBs are indicated by asterisks in the Tables. Otherwise, the reported peak fluxes are obtained by performing forced Gaussian fits at the position of either the radio counterpart seen in another AMI epoch, or at the best-known *Swift* position of the GRB. The flux errors are the errors output by PYSE, added in quadrature to the AMI 5 per cent calibration error (Perrott et al. 2013) and are also primary beam corrected. The significance of the peak fluxes reported by PYSE are also included in these Tables.

4 DISCUSSIONS OF AMI OBSERVED GRBS

In this section, we individually discuss those GRBs with *confirmed* radio afterglow detections with AMI that obey the criteria presented in Section 2.3.1. We then briefly comment on those GRBs that may have been detected in just one AMI epoch, which we classify as *possible* radio afterglow detections, and those GRBs that are coincident with a radio source detected in their deep concatenated image only. We also list those GRBs that appear to be coincident with a steady radio source and discuss the ramifications of such associations.

It is important to note that some of the radio detections discussed in this section were made at early times and may therefore suffer from scintillation effects (for example, see Frail et al. 1997). However, 15.7 GHz is usually above the scattering frequency in a given direction and therefore in the weak scattering regime. This implies that scintillation effects are likely to be minimal (see table 1 of Granot & van der Horst 2014). Of course, this assumption is predicated upon the simple framework of Walker (1998), which assumes a single scattering screen at a fixed distance. It is therefore possible that there are unaccounted scintillation effects that result in flux variations more significant than the quoted $1\sigma_s$ errors.

4.1 New *confirmed* GRB radio afterglows discovered with AMI

This section individually discusses the six GRBs whose *confirmed* radio afterglows were discovered with AMI. In five of the cases, the proposed counterparts fulfil the two criteria for a radio afterglow identification, while the other was identified via concatenating the early and late epochs separately (see Section 2.3.1).

4.1.1 GRB 140305A

GRB 140305A was detected by *Swift* BAT at 15:00:20 UT but, due to a Solar observing constraint, was not followed-up at X-ray or optical wavelengths (Cummings et al. 2014a). As a result only a BAT position with a 1.7 arcmin 90 per cent error circle was obtained for this event. AMI was on-target and observing this GRB for 2 h within 5 min post-burst, followed by 10 subsequent observations ranging from 3 to 5 h in duration up until 2014 April 1. The deep image resulting from the concatenation of 11 observation of this source showed the detection of two sources within the BAT error circle. One of these two sources was NVSS 225809+152439, which lies 3.2 arcmin SE of the BAT position. The second source was uncatalogued and lies only 7.8 arcsec from the BAT position at RA (J2000.0) = 22:57:59.32 (±1.70 arcsec) and Dec. (J2000.0) = +15:27:00.60 (±2.84 arcsec). In the individual epochs, this uncatalogued radio source was not detected until the third AMI observation on 2014 March 8 (2.80 d post-burst), with a $5\sigma_s$ detection of

Table 2. The AMI 15.7 GHz GRB catalogue: GRBs that were not detected with AMI, have a possible steady source association or a concatenated detection.

GRB[a]	Type[b]	Radio[c] Flag	Telescope[d]	Date[e] (yyyy-mm-dd)	Start[f] (MJD)	Integration[g] (hours)	Days[h] (post-burst)	Peak Flux[i] (mJy beam^{-1})	Sig[j]	rms[k] (mJy beam^{-1})
120305A	S	N	XRT	2012-03-05	55991.82	1.0	0.00 (4.32)	0.16 ± 0.25	2.6	0.17
120305A	S	N	XRT	2012-03-06	55992.60	1.0	0.78	0.07 ± 0.05	1.9	0.10
120305A	S	N	XRT	2012-03-07	55993.64	1.0	1.83	0.63 ± 2.77	1.6	0.17
120305A	S	N	XRT	2012-03-08	55994.66	1.0	2.84	−0.0 ± 0.0	2.3	0.11
120305A	S	N	XRT	2012-03-09	55995.76	1.0	3.94	−0.04 ± 0.05	2.9	0.12
120305A	S	N	XRT	2012-03-10	55996.68	1.0	4.86	0.26 ± 0.09	2.4	0.11
120305A	S	N	XRT	2012-03-11	55997.74	1.0	5.93	0.13 ± 0.19	1.7	0.22
120305A	S	N	XRT	2012-03-12	55998.62	1.0	6.81	−0.27 ± 0.53	2.4	0.17

Notes. All GRB observations from GRB 130813A onwards followed the updated ALARRM strategy (see Section 2.1).
[a]GRB discovery flag: †: *Fermi* discovered GRB; ‡: *INTEGRAL*-discovered GRB.
[b]GRB type: S – short, L – long.
[c]Radio detection flag: R – radio afterglow first detected with another radio telescope; S – AMI-detected coincident radio source is likely steady; C – coincident radio source detected in the AMI concatenated image; CS – coincident radio source detected in AMI concatenated image that is confirmed to be a steady source; N – no detection.
[d]Best *Swift* telescope position used to search for a radio counterpart: BAT – *Swift* Burst Alert Telescope; XRT – *Swift* X-ray Telescope; UVOT – *Swift* Ultraviolet/Optical Telescope. For GRB 130521A, the best optical position provided by Skynet/PROMPT (James et al. 2013) was used instead.
[e]Date of the AMI observation in yyyy-mm-dd. Concat – concatenation of all epochs with the same pointing.
[f]Start date of the AMI observation in modified julian date (MJD) format.
[g]AMI observation length in hours.
[h]Number of days post-burst since the start of the AMI observation. The response time, in minutes, has also been included in brackets for those AMI observations that began ≤0.01 d post-burst.
[i]Peak flux density as reported by PYSE. The '*' symbol indicates those GRBs for which the listed AMI peak flux is the measured flux of a radio source detected above a $4\sigma_s$ significance, coincident with the best-known *Swift* position of the GRB (i.e. within $3\sigma_p$). All other listed fluxes are derived from a forced Gaussian fit at the best-known *Swift* position. The $1\sigma_s$ error bar is the flux error output PYSE, added in quadrature to the AMI 5 per cent calibration error.
[j]The significance of the AMI flux reported by PYSE, which are measured in units of σ_s above a local rms. (Note that the PYSE-fitting algorithm failed on the 2012-04-05 and 2012-04-08 observations of GRB 120311A and all of the GRB 121128A. The forced fits were conducted using MIRIAD and the reported significance is just the forced fitted peak flux divided by the global rms reported in the last column.)
[k]The global rms of the middle quarter of the AMI image.
(The full table is available in the online journal in a machine-readable and PDF form. A portion is shown here for guidance.)

0.29 ± 0.06 mJy beam^{-1}. A further five AMI observations detected this radio source with a flux significance between $4.6 < \sigma_s < 6.9$ until it dropped below detectability on 2014 March 30 (25 d post-burst). The light curve of GRB 140305A can be found in Fig. 1. Given that the most sensitive AMI non-detection on 2014 March 30 would have detected the brightest flux measurement of 0.42 ± 0.06 mJy beam^{-1} (observed on 2014 March 15) with a $\sim 6\sigma_s$ significance, we identify this uncatalogued radio source as transient and likely the radio counterpart to GRB 140305A.

4.1.2 GRB 140629A

AMI-monitored GRB 140629A nine times from 1.27 until 23.16 d post-burst. A blind search of the deep concatenated image detected a $5.0\sigma_s$ source with flux 0.10 ± 0.02 mJy beam^{-1} within $1.4\sigma_p$ of the UVOT position. However, no sources were blindly detected in the individual epochs. We therefore concatenated the four earliest AMI observations of GRB 140629A ranging between 2 and 6 d post-burst, and the four latest observations between 7 and 23 d post-burst, to search for transient behaviour using the technique described in Section 2.3.1. The first concatenated epoch detected a radio source coincident with that detected in the deep concatenated image but with a brighter flux of 0.15 ± 0.03 mJy beam^{-1} at a $5.2\sigma_s$ significance. The second concatenated epoch had a comparable rms noise to the first concatenated epoch but no coincident radio source was detected down to a $4\sigma_s$ upper limit of 0.09 mJy beam^{-1}. This analysis demonstrates that GRB 140629A obeys criterion (ii) in Section 2.3.1, suggesting the coincident radio source was transient in nature, and therefore likely the radio afterglow of GRB 140629A, which faded below detectability at $\gtrsim$6 d post-burst.

4.1.3 GRB 140709A

The XRT position of GRB 140709A lies 30.1 arcsec from the NVSS 201841+511349, which has an integrated flux of 1.13 ± 0.06 mJy beam^{-1} at 15.7 GHz based on the concatenated AMI image. During the 2014 July 11 AMI observation of GRB 140709A, which took place 2.9 d post-burst, a radio source began to appear at the GRB XRT position. However, due to the AMI-LA resolution of 30 arcsec, this potential radio afterglow was blended with NVSS 201841+511349. In order to investigate whether this new radio source was real, CASA was used to subtract a model of the contribution of the NVSS source from the visibilities. The resulting image revealed an unresolved point source at the position of the GRB with a peak flux of 0.46 ± 0.05 mJy beam^{-1} (Anderson et al. 2014d). This same technique was performed on all the AMI observations, showing the detection of a fading point source present in two subsequent observations (see Fig. 1), fading below detectability by 2014 July 18. For those AMI observations for where radio afterglows were detected, forced fit fluxes were obtained manually using the radio reduction software MIRIAD (Sault, Teuben & Wright 1995). The reported significance on these forced fits reported in Table 1 correspond to the forced fit flux divided by the rms noise (which is why some of these values are negative). We therefore identify this transient radio source as the likely radio afterglow of GRB 140709A. While no other radio detections were reported, the optical counterpart detected by Castro-Tirado et al. (2014b) was faint, and further studies indicate that this GRB may be a member of the 'dark' burst population (Littlejohns et al. 2015). Several proposed suggestions for their dark nature may be due to an intrinsically faint optical counterpart, that they reside in high-redshift galaxies, or that

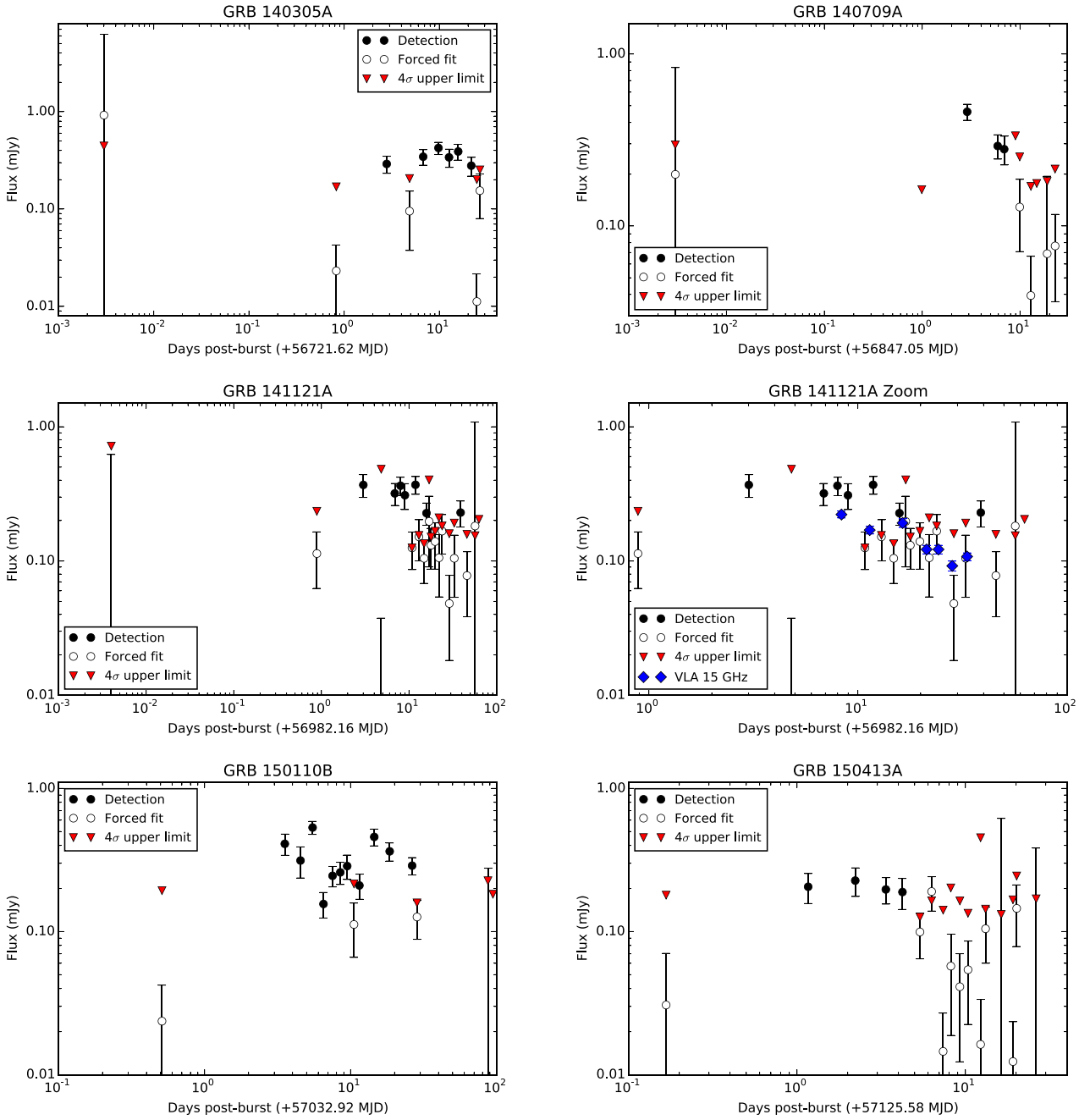

Figure 1. The AMI 15.7 GHz light curves of new *confirmed* GRBs discovered with AMI. The black data points are the $>4\sigma_s$ AMI detections of the GRB radio afterglows. The open circles are the fluxes measured from a point source force-fitted at the position of the GRB in those AMI data sets for which there was no detection. In some cases, the flux measured from the forced fit, and/or the negative error-bar, are consistent with zero and were therefore either not depicted or extend lower than the y-axis). The $4\sigma_s$ upper limits on the non-detections are also illustrated (red triangles). The light curve of GRB 141121A is plotted twice, the second plot zooming in at late times ($\geq$1 d post-burst) so as to better discern the light-curve structure, while also including VLA 15 GHz detections (Cucchiara et al. 2015). All error-bars are $1\sigma_s$.

their optical emission is obscured by dust and gas extinction in their host galaxies (e.g. van der Horst et al. 2009).

4.1.4 GRB 141121A

GRB 141121A is a member of the newly established class of ultra-long GRBs (UL-GRBs), which have prompt γ-ray emission lasting for $\gtrsim$1000 s (e.g. Virgili et al. 2013; Evans et al. 2014; Levan et al. 2014). Through the ALARRM trigger, AMI was on-target and observing GRB 141121A just 6 min post-burst with a follow-up observation occurring 0.9 d post-burst. It was not until 2014 November 24, 3 d post-burst, that AMI detected the radio counterpart to GRB 141121A, resulting in a flux of 0.37 ± 0.07 mJy beam^{-1}. This is the first and earliest reported detection of the radio counterpart to GRB 141121A (Anderson et al. 2014c), which was then observed

and detected with the WSRT at 4.9 GHz (van der Horst 2014) and the VLA at 6.2 and 14 GHz (Corsi 2014c; Corsi et al. 2014). Fig. 1 shows the AMI light curve of GRB 141121A. A multiwavelength analysis of GRB 141121A has also been conducted by Cucchiara et al. (2015).

A zoomed in light curve beginning ∼1 d post-burst that includes the 15.7 GHz VLA detections (Cucchiara et al. 2015) can be found in Fig. 1. The AMI detections, forced fits and upper limits, are consistent with the VLA detections, but the AMI observations also show evidence for radio rebrightening at ∼12 and ∼39 d post-burst (note that the AMI detection at 39 d is within $3\sigma_s$ of the VLA detection at 33 d, but both detections show the 15.7 GHz flux is increasing at late times). Cucchiara et al. (2015) demonstrated that around 3 d, when the 15.7 GHz flux is near its peak, at least 50 per cent of the radio flux is being contributed by the reverse-shock. The flatness of the AMI light curve up to 12 d post-burst, followed by evidence for late time rebrightening, may support the detection of multiple peaks from the forward- and reverse-shock at 15.7 GHz. Energy injections, which is supported by the detection of flares and plateaus in the XRB light curve of GRB 141121A (Cucchiara et al. 2015), could also cause radio light-curve flattening (Frail et al. 2004). However, this flatness may also be an artefact of the radio counterpart being close to the AMI detection limit. The VLA light curves presented in Cucchiara et al. (2015) also show late-time radio modulations, particularly at lower-frequencies, which they attribute to scintillation. While the AMI observing frequency is in the weak-scattering regime, it may still be contributing towards the fluctuations. However, such scintillation is unlikely to be significant enough to explain the variations seen in the GRB 141121A light curve.

4.1.5 GRB 150110B

The ALARRM trigger on GRB 150110B resulted in the first AMI observation occurring at 0.5 d post-burst, when the source had risen above the horizon. AMI then detected the radio counterpart to GRB 150110B on 2015 January 14, corresponding to 3.54 d post-burst, with a flux of 0.41 ± 0.07 mJy beam^{-1} (Anderson et al. 2015c). No optical counterpart was detected for this GRB, but the limits are not particularly constraining (Kuin & Evans 2015; Mazaeva et al. 2015). This radio counterpart remained detectable up until 27 d post-burst during which it showed periods of rapid variability (see Fig. 1). The brightest detection with AMI was on 2015 January 16, 5.5 d post-burst, displaying a flux of 0.53 ± 0.06 mJy beam^{-1}, which then rapidly dropped by a factor of 3 when observed only 1 d later, implying a steep temporal index of $\alpha = -9 \pm 1$ (for flux $F(t) \propto t^{\alpha}$). The radio flux then took another 8 d to peak again, 14.5 d post-burst at 0.46 ± 0.06 mJy beam^{-1}, before it faded below detectability ∼28 d post-burst. It is possible that this variability could have been caused by scintillation, which has been shown to be significant for many GRBs, in some cases with modulations >100 per cent (for example, see Frail et al. 2000). Scintillation is a reasonable assumption for this event as in the direction of GRB 150110B, the transition frequency at which the scattering strength is unity is $\nu_0 \approx 20$ GHz, placing 15.7 GHz in the strong scattering regime (Walker 1998).

4.1.6 GRB 150413A

ALARRM had AMI on-target and observing GRB 150413A when the source had risen above the horizon at 0.17 d post-burst. The follow-up observation that took place on 2015 April 14, just 1.2 d post-burst, resulted in the detection of a coincident radio source with a flux of 0.21 ± 0.05 mJy beam^{-1} (Anderson et al. 2015a,b). The source remained detectable until 2015 April 17, after which it dropped below the AMI sensitivity (see Fig. 1). In the GRB rest frame, these four detections occurred within ∼1 day post-burst so it is possible we detected the reverse-shock radio peak. The most sensitive late time AMI observation proceeding the detections on 2015 April 29 would have detected the brightest flux (from the 2015 April 15 observation) at a $6\sigma_s$ level, indicating transient behaviour. We therefore suggest that this coincident radio source is the radio afterglow of GRB 150413A. The only other radio observation reported for this event was using the Nanshan 25m radio dish in the pulsar search mode, the purpose of which was to search for an associated FRB(s), but no results were included (Xu et al. 2015). GRB 150413A also had a bright optical counterpart (e.g. Tyurina et al. 2015) and Gorbovskoy et al. (2016) searched for early-time optical polarization, but none was detected. The flux forced fitting in the AMI non-detections was performed at the optical position provided by Ivanov et al. (2015).

4.2 *Confirmed* radio-detected GRBs detected with AMI

This section individually discusses the seven radio-detected GRBs that were detected by AMI. We define 'radio-detected GRBs' as those for which the radio afterglow was first reported from a detection made with a telescope other than AMI. The detection must have been reported in the GCN or in the literature, and not subsequently reclassified as a steady radio source. These GRBs also obey the *confirmed* radio afterglow selection criteria presented in Section 2.3.1.

4.2.1 GRB 120326A

GRB 120326A was the first GRB detected by AMI as part of the ALARRM programme. ALARRM triggered AMI on this object at 0.31 d post-burst, after this object had risen above the horizon, obtaining a $4\sigma_s$ upper limit of 0.56 mJy beam^{-1}. It was then detected during the second AMI observation of this event at 7.15 d post-burst as seen in Fig. 2 (during the early stages of the ALARRM programme the follow-up AMI GRB monitoring observations were not very uniform in time). However, GRB 120326A was detected at very early times at 230 GHz with the Sub-Millimeter Array (SMA; Urata et al. 2014) just 0.53 d post-burst, with a flux of 2.84 ± 0.86 mJy beam^{-1}, yielding one of the earliest sub-mm detections of a GRB. Using this value and the first AMI limit (at 0.31 d), we can calculate a rough early-time lower limit on the spectral index, which was $\beta > +0.6$ (for $F(\nu) \propto \nu^{\beta}$) at the $4\sigma_s$ level, indicating that self-absorption was playing a role above 15.7 GHz during this time. Radio detections were also made with CARMA at 92.5 GHz at 4.55 d post-burst (Perley, Alatalo & Horesh 2012) and the VLA at 21.9 GHz at 5.45 d post-burst (Laskar, Zauderer & Berger 2012), yielding fluxes of 3.2 ± 0.4 and 1.36 mJy beam^{-1}, respectively.

The AMI flux measurements of GRB 120326A were first reported by Staley et al. (2013). However, the flux values for GRB 120326A presented in this publication, calculated using our new and improved reduction and analysis pipeline, are slightly different due to updated scripts for the AMI data reduction process used in AMI-REDUCE and the application of more stringent protocols for acceptable data sets. For example, the AMI observations of GRB 120326A that took place on 2012-04-04 and 2012-04-08, which are mentioned in Staley et al. (2013), were rejected from further analysis due to being rain affected data sets.

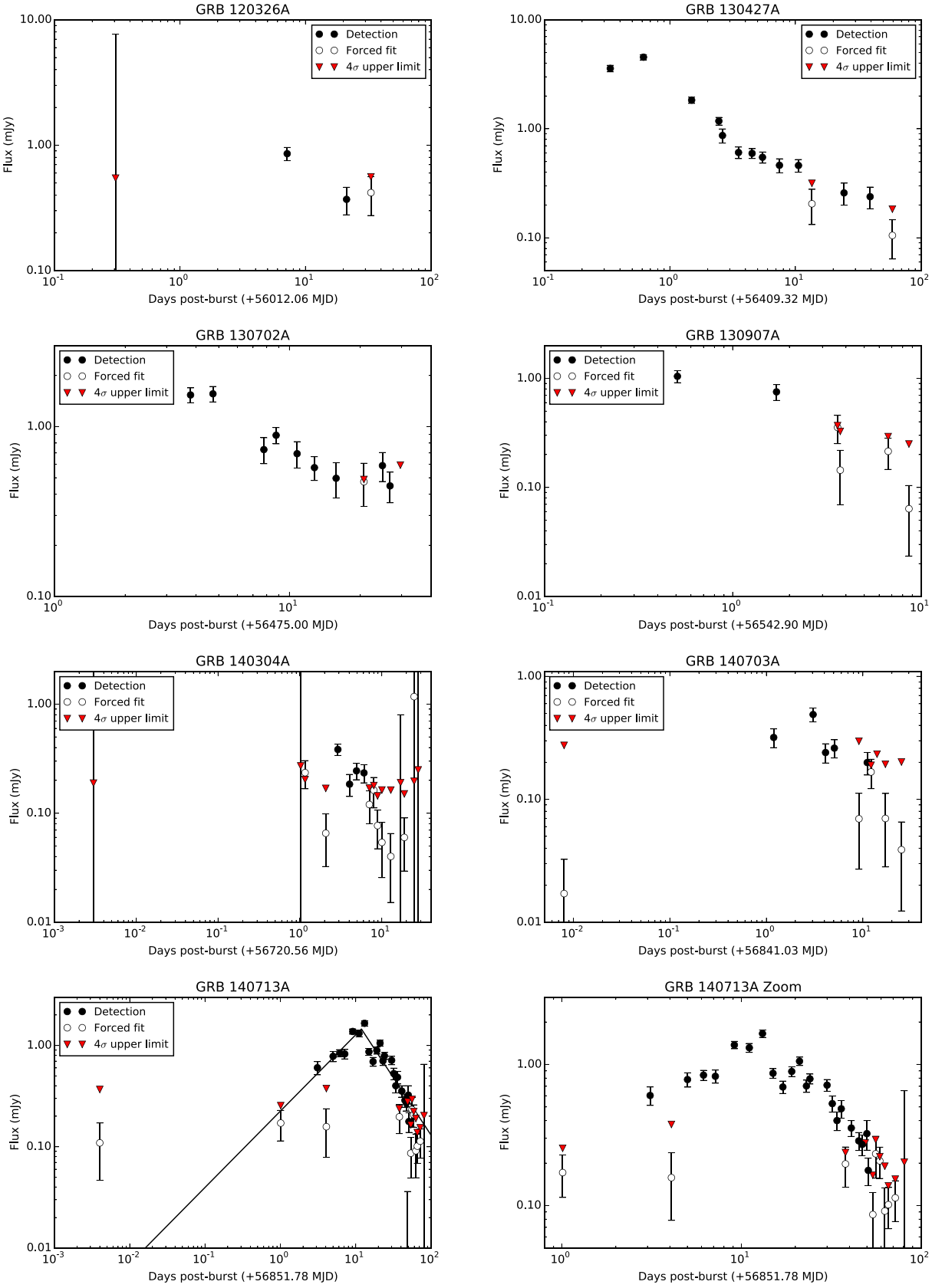

Figure 2. As for Fig. 1 plotting AMI detections of the *confirmed* radio-detected GRB afterglows. The light curve of GRB 140713A includes a broken power-law fit to the radio detections. A zoomed in plot of GRB 140713A at late times (≥1 d post-burst) is also included to better discern the light-curve structure.

4.2.2 GRB 130427A

The close proximity ($z = 0.34$; Flores et al. 2013; Levan et al. 2013; Xu et al. 2013c) of GRB 130427A, and therefore its bright multi-wavelength counterpart, made it an excellent candidate for studying the forward-reverse shock scenario, particularly in the radio band (i.e. Laskar et al. 2013; Anderson et al. 2014e; Perley et al. 2014b; van der Horst et al. 2014). Through the ALARRM programme, AMI triggered on this GRB and was on-target and observing 0.34 d post-burst, as soon as GRB 130427A had risen above the horizon, resulting in one of the earliest published radio detections of a long GRB (Anderson et al. 2014e). Further AMI observations beginning at 0.62 and 1.49 d post-burst then revealed a peak and rapid decay, demonstrating the early-time radio emission was likely dominated by the reverse-shock component at 15.7 GHz (see the light curve in Fig. 2). The AMI fluxes for GRB 130427A displayed in Table 1 are slightly different to those quoted in Anderson et al. (2014e), as they were calculated using the pipelined automated technique with a $4\sigma_s$ detection significance described in this paper rather than through a manual analysis using MIRIAD. However, the flux values from both analyses agree within their $1\sigma_s$ flux errors.

4.2.3 GRB 130702A

GRB 130702A was detected with both the *Fermi*-GBM and *Fermi*-LAT (Cheung et al. 2013) and quickly localized by the Intermediate Palomar Transient Factory (iPTF; Rau et al. 2009; Kulkarni 2013) through the discovery of its optical counterpart iPTF13bxl, which is the first afterglow identification based solely on a *Fermi*-GBM detection (Singer et al. 2013). GRBs detected with *Fermi*-LAT are quite unusual, as this instrument is sensitive to events that produce much higher energy γ-rays than those produced by GRBs detected by *Swift*-BAT and the *Fermi*-GBM. As its counterpart localization was not reported until 1.3 d post-burst, many of the usual GRB multiwavelength follow-up programmes did not commence until 2 d post-burst. The first radio detection was with CARMA between 2.0 and 2.2 d post-burst, reporting a flux of $\sim$2 mJy beam^{-1} at 93 GHz (Perley & Kasliwal 2013), and was quickly followed by detections with the WSRT, VLA and GMRT (Chandra 2013; Corsi, Perley & Cenko 2013; van der Horst 2013). See Singer et al. (2013) for further details and the analysis of the VLA and CARMA observations.

The first observation, and consequently detection, of GRB 130702A obtained with AMI was of 2 h duration and took place 3.8 d post-burst, with follow-up observations being regularly obtained every 2 or 3 d. The radio counterpart continued to be detectable with AMI up until 2013 July 28, with the final observation taking place on 2013 July 31. A light curve of the AMI detections of GRB 130702A can be found in Fig. 2, and a detailed analysis of the AMI and WSRT radio light curves will be presented in van der Horst et al. (in preparation).

4.2.4 GRB 130907A

GRB 130907A is another one of the small number of *Swift*-detected GRBs that has also been detected with *Fermi*-LAT (Vianello et al. 2013; Vianello 2013). It has also been classified as a dark burst, where the optical flux attenuation was likely caused by a high quantity of dust extinction ($A_V > 1$; Littlejohns et al. 2015). A VLA observation at 24.5 GHz was obtained just 4 h post-burst, detecting the counterpart with a flux of $\sim$1.2 mJy beam^{-1} (Corsi 2013). This represents one of the earliest radio detections of a GRB to date (see table 2 of Anderson et al. 2014e) and the earliest VLA detection of a GRB (Veres et al. 2015). The ALARRM triggered AMI observation began when the source had risen above the horizon 0.51 d post-burst. This observation was 2 h in duration and detected the radio counterpart with a flux of 1.04 ± 0.13 mJy beam^{-1}, again providing one of the earliest recorded radio GRB detections (Anderson et al. 2013). Follow-up AMI observations were then manually scheduled every 1–2 d for a duration of 2–4 h until 2013 September 16, yet only the observations on 2013 September 8 and 9 provided a firm detection (see Fig. 2).

The early-time radio detections obtained with AMI (Anderson et al. 2013) and the VLA (Corsi 2013) made GRB 130907A a prime candidate for investigating contributions from the reverse-shock. However, radio modelling of multifrequency VLA observations by Veres et al. (2015, see their fig. 1) show that while the data can be modelled by the combination of a forward- and reverse-shock, it is not constraining enough to determine if the reverse-shock component is truly necessary. However, based on the 15.7 GHz extrapolated light curve in fig. 6 of Veres et al. (2015) it appears that our first AMI detection at 0.51 d post-burst occurred around the peak in that radio band. This peak time is even earlier than the 15.7 GHz peak observed from GRB 130427A, which occurred around 0.6–0.9 d post-burst and was well described by a reverse-shock model component (Anderson et al. 2014e; Perley 2014b), so such a scenario should not be ruled out.

4.2.5 GRB 140304A

Following the initial detection of GRB 140304A with *Swift*, early-time follow-up observations were conducted with several radio telescopes. ALARRM triggered on this GRB and had AMI on-target and observing GRB 140304A less than 5 min post-burst, resulting in a $4\sigma_s$ flux upper limit of 0.19 mJy beam^{-1}. Further AMI observations of GRB 140304A were scheduled daily until 2014 March 14, when a reduce observing cadence was implemented until 2014 April 1. This high-redshift GRB ($z = 5.283$; Jeong et al. 2014) was also simultaneously detected with the VLA and CARMA, just 0.45 d post-burst resulting in 5.8 GHz and 85 GHz fluxes of $\sim$0.05 and $\sim$0.5 mJy beam^{-1}, respectively (Laskar, Zauderer & Berger 2014a; Zauderer, Laskar & Berger 2014b).

AMI first detected GRB 140304A at 2.91 d post-burst with all following detections showing the flux to be decreasing. The non-detection less than 1 d prior to the first detection, with a $4\sigma_s$ upper limit of 0.17 mJy beam^{-1}, suggests a power-law temporal index of $\alpha > +2.4$ for flux $F(t) \propto t^{\alpha}$. The full light curve can be found in Fig. 2. The high redshift of this GRB implies that the rest-frame time for the first AMI detection occurred at $\sim$0.5 d post-burst. Given this steep flux increase, it is possible that AMI may have detected the reverse-shock peak in the radio band. Further broad-band modelling is required to investigate this suggestion.

4.2.6 GRB 140703A

ALARRM rapidly triggered on this *Swift* event and pointed AMI at the position of GRB 140703A within 12 min post-burst, resulting in a $4\sigma_s$ upper limit of 0.27 mJy beam^{-1} after 2 h of integration (Anderson et al. 2014b). GRB 140703A was then rapidly detected in the radio band with the VLA and CARMA, obtaining radio afterglow detections at 19 and 93 GHz just 0.35 and 0.67 d post-burst, resulting in fluxes of $\sim$0.28 and $\sim$2 mJy beam^{-1}, respectively (Corsi 2014a; Perley 2014d). Follow-up AMI observations between

4 and 6 h in duration were then manually scheduled to occur every 1 or 2 d up until 2014 July 20, with a final observation on 2014 July 28. The radio afterglow was clearly detected ($>4\sigma_s$) with AMI between 1.19 and 11.10 d post-burst, and appeared to peak ∼3 d post-burst. This peak corresponds to a rest-frame time of 0.7 d post-burst, once again suggesting a possible reverse-shock origin. The light curve then steadily declined until ∼12 d post-burst, at which point it dropped below detectability (see Fig. 2).

4.2.7 GRB 140713A

GRB 140713A has been detected in both the radio (Anderson et al. 2014a; Zauderer, Fong & Berger 2014a) and X-ray bands (Stamatikos et al. 2014) but not at optical wavelengths. Deep photometric observations yielding non-detections suggest that this GRB may be a dark burst (Castro-Tirado et al. 2014c). AMI was on-target and observing GRB 140713A less than 6 min post-burst, obtaining a $4\sigma_s$ upper limit of 0.37 mJy beam^{-1}. The earliest radio detection was obtained with CARMA at 85 GHz, just 0.49 d post-burst, yielding a peak flux of 1.5 ± 0.3 mJy beam^{-1} (Zauderer et al. 2014a). The first AMI detection of GRB 140713A was 3.1 d post-burst and we continued to observe this event every 1–3 d for 2–6 h until 2014 September 23, with the last observation taking place on 2014 October 2 (see the full light curve in Fig. 2). The brightest AMI detection occurred at 13 d post-burst, with a flux of 1.65 ± 0.10 mJy beam^{-1}, with a possible second peak at 21 d (see the zoomed version of the light curve in Fig. 2). A broken power-law fit to the AMI light curve gives a rising slope of $\alpha = +0.75 \pm 0.11$ and a decay slope of $\alpha = -1.13 \pm 0.06$ for $F(t) \propto t^{\alpha}$, showing a peak flux of 1.45 ± 0.36 mJy beam^{-1} at 11.92 ± 1.10 d post-burst ($\chi^2_{red} = 5.17$). This peak time is typical of the forward-shock emission often observed at 15.7 GHz (see modelling in Ghirlanda et al. 2013). A full modelling of the AMI light curve, in conjunction with WSRT observations, will appear in van der Horst et al. (in preparation), which will give a thorough multiwavelength analysis of this GRB.

4.3 New *possible* GRB radio afterglows discovered with AMI

There were six GRBs that yielded a radio detection in only one AMI epoch. In each case, the detection had a flux significance of $4 \leq \sigma_s < 5$, with late time constraining upper limits that would have detected this source with a $\geq 5\sigma_s$ significance. Even so, we only consider these events as *possible* GRB radio afterglows. The GRBs that fall into this category include GRB 120320A, GRB 130625A, GRB 140209A, GRB 140318A, GRB 140320C and GRB 140607A (the latter four were observed during the updated observing strategy that began in 2013 August). The most convincing *possible* radio afterglow detections are from GRB 130625A, GRB 140318A and GRB 140320C. GRB 140318A has also been classified as an optically dark burst (Littlejohns et al. 2015), and its AMI light curve can be found in Fig. 3. A summary of each of these six GRBs can be found in Appendix A.

4.4 AMI concatenated detections

There are also several GRBs for which no coincident radio source was detected in a single epoch but one was detected in the deep concatenated image. In such cases, it is possible that combining the individual epochs to create a deep concatenated image provided the sensitivity required to detect the radio afterglow. Combining the early- and late-time AMI epochs into two concatenated

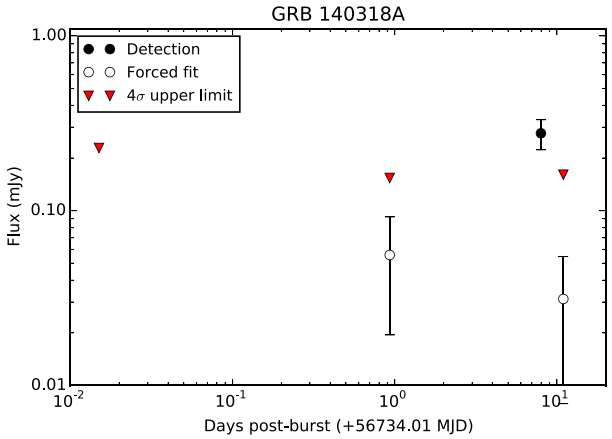

Figure 3. The AMI 15.7 GHz light curve of GRB 140318A. The black data point is the $>4\sigma_s$ AMI detections of GRB 140318A. The red triangles show the $4\sigma_s$ rms noise levels of all four AMI epochs. All errors are $1\sigma_s$.

images allowed us to confirm the detection of the radio afterglow from GRB 140629A (see Sections 2.3.1 and 4.1.2). However, this technique did not work for GRB 130606A, GRB 140508A, GRB 140801A and GRB 150309A as the resulting images were either not sensitive enough to detect the radio source identified in the full concatenated image, or the flux of the coincident radio source agreed between the two concatenated images indicating that it was likely steady. These GRBs are described in Appendix B.

If not radio afterglows, these coincident radio sources are likely serendipitous rather than radio emission from star formation in their host galaxies (for example, see Berger et al. 2003). Most claimed associations have been recently ruled out by sensitive late-time radio observations, which demonstrate that previous radio detections were likely of long-lived radio afterglows, or noise fluctuations or reduction artefacts, rather than from star formation (Perley et al. 2017).

4.5 Radio-detected GRBs that were not detected with AMI

There were eight *Swift* radio-detected GRBs identified during the old ALARRM observing strategy that ran between 2012 March and 2013 August. However, of these eight only GRB 120326A and GRB 130427A were detected with AMI. The radio-detected GRBs that were not detected with AMI during this period were GRB 120404A, GRB 120422A, GRB 120521C, GRB 130131A, GRB 130418A and the short burst GRB 130603B (Zauderer, Berger & Laskar 2012a; Zauderer, Laskar & Berger 2012b; Laskar, Zauderer & Berger 2013b; Zauderer, Berger & Laskar 2013; Perley 2013; Fong et al. 2014; Laskar et al. 2014). It is highly likely that our lack of AMI detections of radio GRBs during this period is owed to the short 1 h integrations that were specific to the old ALARRM observing strategy. The radio afterglows were likely below the $4\sigma_s$ sensitivity limit, which is usually between 0.3 and 0.7 mJy beam^{-1} for a 1 h observation.

However, only 4 out of the 13 *Swift* radio-detected GRBs were not detected with AMI during the period of the new ALARRM strategy, between 2013 August and 2015 April. GRB 140419A, GRB 140515A and GRB 141026A likely went undetected due to the AMI 4 h sensitivity limit of ∼0.2 mJy beam^{-1} ($4\sigma_s$). The fourth event, GRB 140309A, had an unconfirmed detection during the first AMI epoch at 0.93 d post-burst, but its proximity to NVSS 155207+273501 means we cannot rule the possibility of it being an artefact. This flux density, along with the forced fitted flux densities

derived for the rest of the observations of these GRBs, can be found in Table 2. Individual descriptions of these four GRBs, along with GRB 130603B (an interesting case), can be found in Appendix C.

4.6 Coincident steady sources

There are five GRBs that are coincident, or in close proximity of, an uncatalogued radio source detected with AMI, which are likely steady. These include GRB 130216A, GRB 140320B, GRB 140606A, GRB 141015A and GRB 141020A. The measured source flux densities of these GRBs are included in Table 2 and a detailed description of these observations can be found in Appendix D. Once again, these associations are likely to be serendipitous chance coincidences with radio cores or lobes from unrelated galaxies.

5 RADIO GRB STATISTICAL DISCUSSIONS

5.1 Radio GRB detection rates

The current best estimate of the radio detection rate of *Swift* GRBs is 29 per cent, which is based on a comprehensive investigation of all GRBs observed in the radio band between 1997 and 2011 by Chandra & Frail (2012). However, as previously mentioned, it is possible that this detection rate may be biased due to radio follow-up often being based on some prior knowledge of the GRB's properties, with often the additional incentive of performing multiwavelength studies with data at other wavelengths. In fact, only 28 per cent of *Swift* GRBs in their sample were observed at radio wavelengths, which means only 8 per cent of *Swift* GRBs before 2011 have confirmed radio afterglows.

The ALARRM project has now gathered a far more unbiased sample of radio observations of *Swift* GRBs where the only constraint is whether the explosion is within the observable AMI sky. However, the early strategy, though triggering on all *Swift* GRBs with a declination $> -10^{\circ}$, did not yield many detections. All triggered and monitoring AMI observations were 1 h in duration, resulting in an rms of $\sim$0.1 mJy beam^{-1}. We know from fig. 4 of Chandra & Frail (2012) that the majority of radio-detected GRBs prior to 2011 had peak fluxes between 0.1 and 0.2 mJy beam^{-1}, so 1 h AMI observations were not sensitive enough to detect most radio afterglows. As a result, we only detected 2 out of the 8 *Swift* radio-detected GRBs in the AMI sky, which corresponds to a detection rate of 3 per cent for the 67 monitored *Swift* GRBs between 2012 March and 2013 August.

After the ALARRM strategy update in 2013 August, all *Swift* GRBs with a declination $>15^{\circ}$ were observed for 2 h with AMI following the γ-ray trigger, with 4 h follow-up observations at 24 h, 3, 7 and 10 d post-burst (with a higher cadence for those events where we identified the radio afterglow). These longer observations bought the rms noise down to $\sim$0.03–0.04 mJy beam^{-1}, making the programme sensitive to GRBs with radio counterparts $\geq$0.12 mJy beam^{-1}. Between 2013 August and 2015 April, AMI detected 10 ($\sim$70 per cent) out of the 14 radio-detected *Swift* GRBs in the AMI observable sky, 6 of which were discovered with AMI as part of this project (see Section 4.1), thus increasing the rate of GRB radio afterglow detections in this declination range by a factor of $\sim$1.5 over an 18-month period. As the only discriminant for AMI observations was the declination range, we can assume that the sample of the 65 events observed as part of this project between 2013 August and 2015 April are representative of the entire *Swift* GRB sample. Therefore, the radio detection rate is 15 per cent down to a conservative sensitivity limit of $\sim$0.2 mJy beam^{-1} (rms noise for most 4 h observations are 0.03–0.04 mJy beam^{-1}), which is based on radio observations that were not informed by prior knowledge of any GRB multiwavelength properties. By also including the four radio-detected *Swift* GRBs not detected with AMI since the start of the new strategy (see Section 4.5), the radio detection rate increases to 22 per cent but to an unknown completeness limit. If we also include the four *possible* AMI-detected *Swift* GRBs since the start of the new strategy (see Section 4.3), then the total radio detection rate for *Swift* GRBs may be as high as 28 per cent.

Chandra & Frail (2012) report several GRBs with radio peak fluxes $\geq$0.2 mJy beam^{-1}, the majority of which were detected with the VLA prior to its upgrade (typical GRB sensitivity limits of $\sim$0.1–0.15 mJy beam^{-1}, see their table 4). If we assume that the broad-band spectrum of all GRB afterglows in the Chandra & Frail (2012) sample follow 'Spectrum 1' in the modelling performed by Granot & Sari (2002), which is the most relevant for describing GRB afterglows with detectable radio emission in the first days to weeks post-burst (Granot & van der Horst 2014), then the spectral index at 15.7 GHz is likely to be $\beta \sim 2$ or 1/3 (for $F(\nu) \propto \nu^{\beta}$, note that this model assumes a spherical ultra-relativistic blast wave impacting a uniform or wind-like circumstellar medium, Blandford & McKee 1976). As this model requires that $\beta > 0$ in the radio band, we consider AMI capable of detecting all GRBs with reported peak fluxes $\geq$0.2 mJy beam^{-1} for an observing frequency $\leq$15 GHz. AMI would therefore have only detected $\sim$50 per cent of the radio-detected *Swift* GRBs in the Chandra & Frail (2012) sample. This suggests that the radio GRB detection rate at 15.7 GHz may double if the sensitivity is improved by a factor of 2, from $\sim$0.2 mJy beam^{-1} to $\sim$0.1 mJy beam^{-1}. Based on the AMI statistics, the radio-detection rate for *Swift* GRBs could be as high as $\sim$44–56 per cent, down to a sensitivity of $\sim$0.1–0.15 mJy beam^{-1}. This result is supported by assuming the typical log$N$–log$S$ relationship for radio sources ($N \propto S^{-3/2}$; Fomalont 1968), where N is the number of GRBs with fluxes greater than S. Using the ratio of the detection limits, $N \propto (0.125/0.2)^{-3/2} \approx 2$.

Note that there are several caveats associated with this implied AMI detection rate. Chandra & Frail (2012) did not report GRB radio peaks in their table 4 that occurred within 3 d post-burst to avoid contamination from the reverse shock in their statistics. This means that including early-time (<3 d) radio peaks from historical GRBs in this flux comparison may change the potential $\sim$50 per cent AMI detection rate of Chandra & Frail (2012) GRBs. The assumed model 'Spectrum 1' may also only be relevant for radio emission generated by the forward-shock, so does not take into account the possibility of the early-time AMI detections arising from the reverse shock. This model is also only valid for a uniform or wind-like (density drops off with radius) medium and may therefore not be relevant for GRBs that occur in low-density environments similar to that of the interstellar medium. GRBs are also now widely accepted to have jet-like outflows rather than spherical (Sari, Piran & Halpern 1999). This estimate also does not consider how incomplete sampling may affect the numbers (i.e. GRB radio flux peaks missed due to the AMI monitoring cadence or the radio follow-up criteria applied to events in the Chandra & Frail 2012, sample).

The implied AMI detection rate of $\sim$44–56 per cent is consistent with the GRB sample that Ghirlanda et al. (2013) and Burlon et al. (2015) base their synthesized population, which was used to demonstrate that the radio afterglows from all *Swift*-GRBs should be detectable with SKA1-MID (Band 5). Their sample consists of the radio-observed GRBs is the BAT6 sample (BAT6 being the brightest *Swift*-BAT-detected long GRBs that are considered complete with respect to the flux limit; Salvaterra et al. 2012), thus it

can be argued that they represent an unbiased sample of GRB radio afterglow properties (for details on *Swift* GRB selection effects and comparisons to GRBs detected with other instruments, see Qin et al. 2013; Lien et al. 2016).

The advantage of the AMI derived GRB radio detection rate is that it is not biased by prior knowledge of the other electromagnetic properties. Chandra & Frail (2012) demonstrated that the optical brightness of a GRB afterglow is potentially a positive indicator for radio detectability. Since radio follow-up of GRBs is historically biased to those with bright optical counterparts, with the goal of obtaining simultaneous observations across the spectrum, the Chandra & Frail (2012) detection rate is likely to be positively biased. The following two possible conclusions can be drawn from the higher implied radio detection rate obtained with AMI:

(i) The Chandra & Frail (2012) sample does represent the radio detection rate of GRBs at 8.5 GHz, and that the AMI rate is only higher as the GRB radio afterglow emission peaks more brightly at 15.7 GHz (Granot & Sari 2002).

(ii) The AMI rapid-response system allows for the detection of more radio afterglows, as it obtains at least one observation within 24 h of the *Swift* GRB trigger.

In order to investigate the first option, extensive multiwavelength modelling over multiple time-scales are required, which is beyond the scope of this paper. However, given the selective nature of the radio follow-up of historical GRBs, the Chandra & Frail (2012) rate is likely affected by incomplete sampling and may therefore not be directly scalable to 15.7 GHz.

The most likely explanation for the difference between the Chandra & Frail (2012) and implied AMI detection rates may be related to the early-time (<1 d) radio observations made possible by the AMI rapid–response system (second option). Such early-time observations are particularly sensitive to the reverse-shock emission peak, which we know can be at least an order of magnitude brighter than the forward-shock peak (as is the case for GRB 130427A; Anderson et al. 2014e). Of the 18 GRBs, we have classed as *confirmed* or *possible* AMI-detected GRBs (Sections 4.1–4.3) that were observed with AMI at early times, 7 (37 per cent) were detected in the radio band <2 d post-burst, 4 (20 per cent) of which were detected only within this time frame. (The upper limit of 2 d in the observer frame was a natural choice given modelling by Ghirlanda et al. 2013; Burlon et al. 2015, only explore the radio emission from the forward-shock between 2 and 10 d post-burst.) Therefore, radio observations at early times may increase the radio detection rate at least another $\sim$20 per cent, which would raise the (Chandra & Frail 2012) detection rate to a value consistent with the implied AMI detection rate (down to $\sim$0.1–0.15 mJy beam^{-1}).

The AMI-ALARRM results therefore demonstrate that early-time radio observations of GRBs play an important role in constraining the radio afterglow detection rates, as they are particularly sensitive to the reverse-shock emission. This strongly suggests that contributions from the reverse-shock component must be considered in future population synthesis and modelling. As both the AMI and Chandra & Frail (2012) GRB samples display radio detections and upper limits with comparable luminosities (see Section 5.3), it is highly unlikely that we have reached the sensitivities necessary to discern the true radio GRB detection rate (as also concluded by Chandra & Frail 2012). Assuming that the GRB sample in the Ghirlanda et al. (2013) and Burlon et al. (2015) simulations are representative of an unbiased sample of *Swift*-GRBs, then SKA1-MID (using Band 5) should be sensitive to the radio afterglow produced by the forward-shock from all *Swift*-GRBs, allowing us to determine if there is a dual population of radio-bright and radio-faint GRBs as suggested by Hancock et al. (2013).

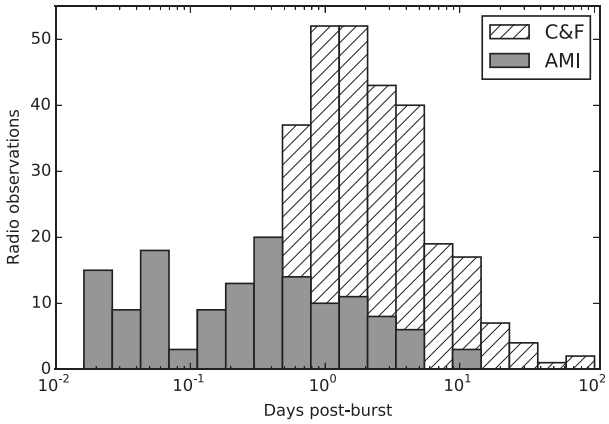

Figure 4. Histogram showing the time post-burst (based on the mid-time of the observation in the observer frame) of the first radio observation of each GRB in the Chandra & Frail (2012) sample (C & F; cross hatched bars) and the AMI sample (grey bars). Neither of these samples includes the radio triggering experiments mentioned in Section 1.

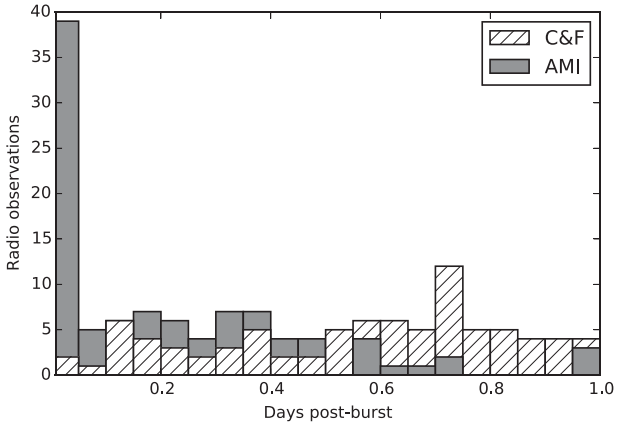

Figure 5. As for Fig. 4 but zoomed in to see those GRBs that were first observed within a day post-burst. It can be clearly seen that the ALARRM programme has enabled some of the earliest responses to GRB alerts on record.

5.2 Early-time radio properties of GRBs

The work of Chandra & Frail (2012) clearly shows that for the last 20 yr radio observations of GRBs have been obtained starting from a few minutes up until 1339 d post-burst. However, the majority of these observations were taken at times later than 10 d post-burst (see fig. 1 of Chandra & Frail 2012), with the earliest observation of each GRB usually occurring after 1 d post-burst (see Fig. 4 and fig. 4 of Veres et al. 2015). However, since the inception of the ALARRM programme, we have obtained 124 AMI observations of 106 GRBs within 1 d post-burst up until 2015 April as indicated in Fig. 4. In fact, 39 of these observations occurred within the first hour following the *Swift* trigger (all based on the mid-time of the observation) using our rapid-response mode (see Fig. 5, which compares the first AMI observations of each GRB observed within 1 d post-burst to the sample from Chandra & Frail 2012, note that Figs 4 and 5 do not include the rapid-response triggers from programmes mentioned in

Section 1 designed to search for prompt, coherent emission, and not the fireball, incoherent emission being probed with AMI). This demonstrates the strength of rapid-response telescope modes compared to relying on manual scheduling.

None of the ALARRM triggered observations with response times within 1 h of the *Swift*-BAT trigger resulted in a detection, with the lowest $4\sigma_s$ limit being 0.19 mJy beam^{-1}. The rapid-response observations are also usually less sensitive than the manually scheduled follow-up observations due to shorter exposure times at less optimum hour angles. However, it is highly likely that the reverse- (and the forward-) shock is too self-absorbed at 15.7 GHz at such early times to be detectable. The only rapid-response AMI triggers that did result in a detection were GRB 130427A at 0.34 d, GRB 130907A at 0.51 d and possibly GRB 120320A at 0.6 d post-burst. These represent some of the earliest radio detections of long GRBs along with a few early VLA detections (see table 2 of Anderson et al. 2014e) including GRB 130907A just 0.193 d post-burst at 19.2 and 24.5 GHz (Veres et al. 2015). Based on these results, it is likely that the radio emission from GRBs does not switch on at 15.7 GHz for several hours following the *Swift*-BAT trigger. Of course, the low redshifts for both GRB 130427A (0.34; Flores et al. 2013; Levan et al. 2013; Xu et al. 2013c) and GRB 130907A (1.24; de Ugarte Postigo et al. 2013c) may also contribute to such early-time detections, as the emission arrival time will be less delayed due to redshift. However, there are also several cases (e.g. GRB 140703A and GRB 150413A, both of which were at a slightly higher redshift of 3.14; Castro-Tirado et al. 2014a; de Ugarte Postigo & Tomasella 2015) where the manually scheduled follow-up AMI observation at around 24 h post-burst did make a detection.

While GRB 140703A and GRB 150413A were at high redshifts, we could have potentially missed the initial radio rise. In order to catch the possible radio turn-on, particularly for low redshift GRBs (e.g. $z < 2$), it may be necessary to further update the ALARRM observing strategy to conduct the rapid-response observation between 4 and 16 h post-bursts (consistent with the early-time AMI detections of GRB 130427A and GRB 130907A), when the potential radio afterglow (forward- or reverse-shock) becomes optically thin at 15.7 GHz. This could be achieved by programming the rapid-response observation to occur when the GRB is at its optimum hour angle, which would also negate some of the sensitivity complications mentioned above. Another options would be to perform a dense number of observations over a 24 h period, which would better capture the GRB switching-on and the potential reverse-shock evolutions (as was seen for GRB 130427A; Anderson et al. 2014e).

In order to estimate the rate of GRB reverse-shock detections made with AMI, we generated a histogram of all the 12 *confirmed* AMI-detected GRBs with respect to days post-burst in the rest frame (days post-burst/(1+z)), where the peak (brightest AMI detection) for each GRB is indicated in black (see Fig. 6). For those AMI-detected GRBs without a redshift, we assumed the average *Swift* redshift of $z = 2.0$ (see Chandra & Frail 2012). This demonstrates that the majority of detections occurred within 10 d post-burst (in the rest frame) with all of the peak detections occurring within 7 d. To investigate whether any of the AMI radio detections were from the reverse-shock, we summarized the rest-frame time of the peak and the earliest and latest radio detections of the 12 AMI-detected GRBs (Table 3). In the rest frame, 6 out of these 12 GRBs peak before 1 d post-burst, including GRB 130427A, which is known to have a reverse-shock radio flare occurring around 0.6 d post-burst (Anderson et al. 2014e). It is therefore possible that AMI has detected the reverse-shock flare of at least 6 GRBs. Another 3 of these 12 GRBs peaked between 1 and 3 d post-burst, with the other 3 peaking at times >3 d post-burst. GRB 130907A, GRB 140304A and GRB 150413A also faded below detectability in 1 d relative to the rest frame. This may suggest that the reverse-shock dominated the radio afterglow for these events (note that multifrequency radio modelling of GRB 130907A was unable to confirm a preference for a forward-reverse shock scenario over a forward-shock-only model; Veres et al. 2015). However, this assumption is an over simplification as the forward-shock peak time (t_p) can occur anywhere within a day to several weeks following the explosions as described by

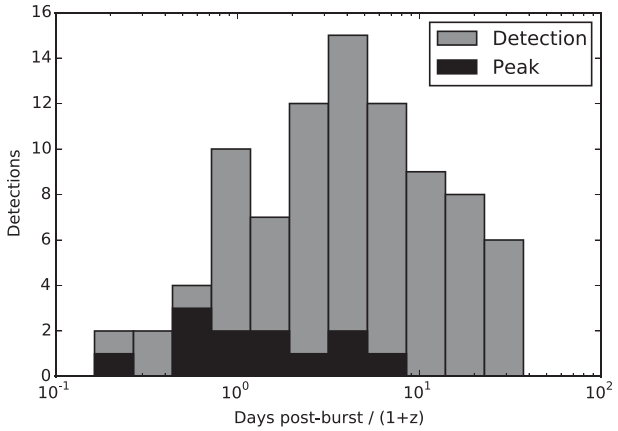

Figure 6. Histogram of the number of GRB AMI detections for a given time post-burst in the rest frame (days post-burst/(1+z)). The brightest or 'peak' detection of each GRB is overlaid in black (which is a subset of the full sample of detections represented in grey). Only 9 out of 12 radio GRBs detected with AMI in two or more epochs have a known redshifts. For those three without redshift measurements, we assume the average redshift of $z = 2$ for radio-detected *Swift* GRBs (Chandra & Frail 2012).

Table 3. Rest-frame times of peak, earliest and latest radio detection of the 12 AMI-detected GRBs.

Detection[a]	≤1 d[b]	1 < d ≤ 3[b]	>3 d[b]
Peak	6	3	3
Earliest	7	4	1
Latest	3	2	7

Notes. We assume $z = 2$ for those GRBs without known redshift measurements (Chandra & Frail 2012).
[a]Refers to the peak (brightest), earliest and latest detection of the radio afterglow for each of the 12 *confirmed* AMI-detected GRBs.
[b]The number of *confirmed* AMI-detected GRBs for which the peak, earliest and latest detection occurred within 1 d, between 1 and 3 d, and later than 3 d post-burst in the rest frame.

$$t_p = 1.93\ F_p^{2/3}\ n_0^{-1/3}\ \varepsilon_{e,-1}^{4/3}\ E_{52}^{-1/3}\ d_{L,28}^{4/3} \left(\frac{(1+z)}{2}\right)^{-1/3} \quad (1)$$

for a homogeneous medium and

$$t_p = 1.55\ F_p^{2/3}\ A_*^{-2/3}\ \varepsilon_{e,-1}^{4/3}\ d_{L,28}^{4/3} \left(\frac{(1+z)}{2}\right)^{-1/3} \quad (2)$$

for a stellar wind medium, where F_p is the peak flux in mJy, n_0 is the circumstellar density for a homogeneous medium, A_* is the density parameter for a stellar wind medium, $\varepsilon_{e,-1}$ is the energy electron fraction divided by 0.1, E_{52} is the isotropic energy in units of 10^{52} ergs, and $d_{L,28}$ is the luminosity distance in units of 10^{28} cm (van der Horst 2007). These equations assume that the self-absorption

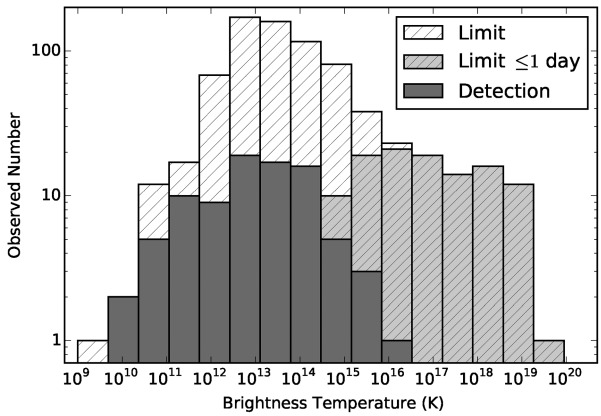

Figure 7. Brightness temperature distribution of the AMI radio afterglow detections for the 12 *confirmed* AMI-detected GRBs (grey filled). We assuming $z = 2$ for those GRBs without redshift measurements. The upper limits on the brightness temperature derived from the $4\sigma_s$ flux limits of the AMI non-detections are also included (white hatches), with the subset of AMI upper limits obtained within 1 d post-burst indicated (grey hatches).

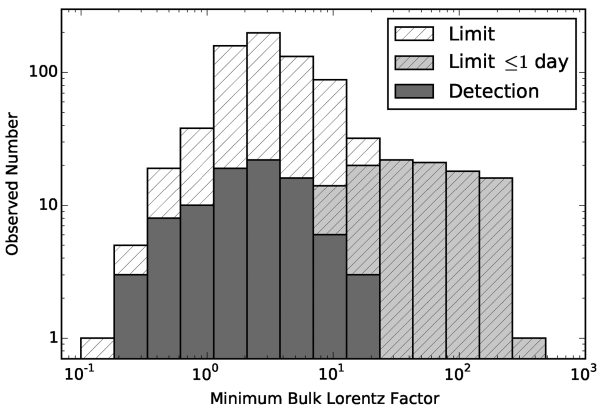

Figure 8. Sameas for Fig. 7 but for the minimum Lorentz factor.

frequency is below 15.7 GHz (for more details on GRB radio light-curve modelling, see Granot & van der Horst 2014, and references therein). Equations (1) and (2) demonstrate that the forward-shock peak is highly dependent on many parameters that can only be calculated through broad-band modelling.

5.2.1 *Brightness temperature and minimum Lorentz factor*

With the growing sample of radio-detected GRBs, along with the early-time (<1 d post-burst) detections and upper limits we are obtaining with AMI, we are able to explore the distribution of GRB brightness temperatures (T_b) and minimum bulk Lorentz factors (Γ) in the radio domain. These values can then be compared to the physical parameters of the blast-wave environment derived from broad-band modelling of GRB afterglows obtained from multiwavelength monitoring campaigns. If we assume that the radiation observed from a GRB is a non-relativistic flow emitted from a region of size ct, then its brightness temperature is

$$T_b = 1.153 \times 10^{-8}\, d^2\, F_\nu\, \nu^{-2}\, t^{-2}\, (1+z)^{-1}\ \mathrm{K}, \quad (3)$$

where d is the luminosity distance to the GRB in cm, F_ν the flux density in Jy, ν is the observing frequency in Hz, t is time in seconds since the γ-ray trigger and z is the redshift (Rybicki & Lightman 1979). (We assume a ΛCDM cosmology using $H_0 = 68\,\mathrm{km\,s^{-1}Mpc^{-1}}$ and $\Omega_m = 0.30$ based on the findings by Planck Collaboration XIII 2016.) However, if the maximum source size ct results in a brightness temperature that exceeds the inverse-Compton limit $T_B \approx 10^{12}$ K in the rest frame, then this assumption is wrong and the GRB outflow is likely relativistic. Given that I_ν/ν^3 (where I_ν is the specific intensity) is a relativistic invariant (Mihalas & Mihalas 1984), the observed brightness temperature is related to the minimum Lorentz factor such that $T_b/T_B = \Gamma^3$ (see similar arguments made by Kulkarni et al. 1998; Galama et al. 1999).

Figs 7 and 8 are histograms of the brightness temperature and minimum Lorentz factor obtained from the AMI detections and upper limits. The radio detections resulted in brightness temperatures ranging from $\sim 2 \times 10^{10}$ to $\sim 8 \times 10^{15}$ K (which is consistent with the range of 10^{13}–10^{16} K proposed by Pietka, Fender & Keane 2015, who used peak luminosity and variability time-scales to constrain the range of T_b for a wide variety of radio flaring objects) and 0.3–20.4 for the minimum Lorentz factors. The upper limits on the brightness temperatures and minimum Lorentz factors calculated using the $4\sigma_s$ flux limits from the AMI non-detections probe a wider range of values, from $\sim 4 \times 10^9$ to $\sim 7 \times 10^{21}$ K and 0.2 to nearly 2000, respectively. Those upper limits obtained from AMI non-detections within 1 d of the initial GRB trigger are represented by grey filled hatched histograms in Figs 7 and 8, dominating the higher end of the upper limit distributions.

Table 4. Highest minimum Lorentz factors obtained from AMI detections.

GRB	Obs frame[a] (days)	Rest frame[b] (days)	T_b[c] ($\times 10^{15}$ K)	Γ[d]	z[e]
130427A	0.36	0.27	4.29	16.24	0.34
130427A	0.64	0.48	1.70	11.94	0.34
130907A	0.55	0.25	7.21	19.32	1.24
140304A	2.99	0.48	1.07	10.22	5.28
140703A	1.27	0.31	2.16	12.93	3.14
150413A	1.28	0.31	1.38	11.14	3.14

Notes. All AMI detections for which the minimum Lorentz factors (Γ) ≥ 10.
[a]Time of the AMI observation in days post-burst in the observer frame.
[b]Time of the AMI observation in days post-burst in the rest (GRB) frame.
[c]Brightness temperature.
[d]Minimum Lorentz factor.
[e]Redshift: Measurements taken from Levan et al. (2013); Xu et al. (2013c); Flores et al. (2013); de Ugarte Postigo et al. (2013c, 2014d); Jeong et al. (2014); Castro-Tirado et al. (2014a); de Ugarte Postigo & Tomasella (2015).

It can be seen that a few of the GRB detections resulted in minimum Lorentz factors (Γ) >10, which have been summarized (along with the corresponding brightness temperature) in Table 4. Each represents the first detection of the GRB (with the exception of GRB 130427A for which the first two detections resulted in $\Gamma > 10$). In the case of GRB 130427A (the first entry in Table 4) and GRB 130907A, these radio detections came from rapid-response observations that were delayed several hours due to the source being below the AMI horizon at the time of the *Swift* detection. These represent some of the earliest detections of a radio afterglow from a long GRB. For comparison with radio GRB detections taken with other telescopes, see table 2 of Anderson et al. (2014e). While these earliest detections of the AMI GRBs in Table 4 range from 0.3 to 3 d post-burst in the observer frame, they correspond to 0.2 and 0.5 d in the rest frame. It is therefore likely that AMI detected the radio counterpart of each of these GRBs just as they were becoming optically thin at 15.7 GHz, with the possibility of it being reverse-shock emission (see caveat in Section 5.2). Overall, this is an excellent

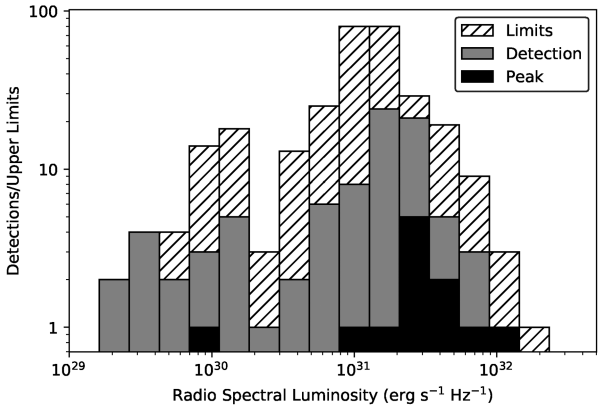

Figure 9. Histogram of k-corrected spectral luminosities and $4\sigma_s$ upper limits of the AMI GRB sample. We assume $z = 2$ for those events without a known redshift. The 12 *confirmed* AMI-detected GRBs are shown in grey. The peak (brightest) AMI detection for each of these 12 GRBs (black; which represent a subset of the detection distribution show in grey) are also included. The $4\sigma_s$ luminosity upper limits (white hatched) are from the AMI observations that are at least 4 h in duration with no detection.

demonstration of how rapid-response systems on radio telescopes allow us to probe early-time brightness temperatures and minimum Lorentz factors in the radio band.

5.3 Radio spectral luminosity

In order to investigate the radio GRB population dichotomy suggested by Hancock et al. (2013), we chose to generate a histogram similar to fig. 4 of Chandra & Frail (2012) but instead looking at the distribution in luminosity (rather than the flux) of the radio detections and $4\sigma_s$ upper limits. (Only 4 h AMI observations with no GRB radio detection are used for the luminosity limits as these are the best illustration of the sensitivity we are achieving with AMI using our current strategy.) Following the same approach as Chandra & Frail (2012), the flux is converted into a spectral luminosity L (erg s^{-1} Hz^{-1}), using $L = 4\pi F d_L^2/(1+z)$, where F is the measured radio flux density and d_L is the luminosity distance calculated from the redshift (z) assuming the same ΛCDM cosmology as described in Section 5.2.1. A k-correction factor of $(1+z)^{\alpha-\beta}$ is also applied, where α and β are the temporal and spectral indices defined by $F \propto t^{\alpha}\nu^{\beta}$, resulting in a k-corrected radio spectral luminosity of $L = 4\pi F d_L^2/(1+z)^{\alpha-\beta-1}$. Similar to Chandra & Frail (2012), we also assume $\alpha = 0$ and $\beta = 1/3$, which is appropriate for an optically thin, flat, post-jet-break light curve (see their section 3.2 and Frail et al. 2006).

Fig. 9 shows the luminosity histogram of the radio detections and $4\sigma_s$ upper limits. The luminosity of the brightest detection (peak) of each of the 12 *confirmed* AMI-detected GRBs is also indicated. If such a dichotomy is possible to discern in AMI data, then the peak from the luminosity distribution of the detections should be clearly separated from the peak of the luminosity upper limit distribution. However, it is clear from Fig. 9 that the peak in the detection, brightest (peak) detection and upper limit luminosity distributions are consistent and show no evidence for a fainter class of radio GRBs down to a sensitivity of 0.2 mJy beam^{-1} at 15.7 GHz. This does not preclude a population dichotomy, as the limits on radio faint GRBs presented by Hancock et al. (2013) using visibility stacking are better than 0.1 mJy beam^{-1} (at 8.46 GHz) for all times with the exception of those within 0.3 d of the initial outburst.

As a further investigation of the luminosity distribution of the AMI-detected GRBs, we plotted the 15.7 GHz spectral luminosity against the time post-burst in the rest frame (see Fig. 10). The AMI luminosity of each of the 12 *confirmed* AMI-detected GRBs, and the corresponding luminosity of the $4\sigma_s$ upper limits, are represented in different colours. The $4\sigma_s$ upper limit luminosities of all other GRB non-detections are included in this plot as white triangles. Once again there is no clear evidence for a dichotomy between the luminosity limits and the GRB detections. This plot also demonstrates that AMI has detected GRBs with wide ranges in spectral luminosities, between $\sim 10^{29}$ to $\sim 10^{32}$ erg s^{-1} Hz^{-1}. However, compared to a similar luminosity plot constructed by Chandra & Frail (2012, see their Fig. 6), we note that AMI has not detected the much fainter GRBs with radio spectral luminosities between $10^{27} - 10^{29}$ erg s^{-1} Hz^{-1}. Such events are known as sub-energetic or low luminosity GRBs (Soderberg et al. 2004) and are extremely rare with only a handful known (see Margutti et al. 2013, and references therein), possibly representing a different GRB population (for example see Liang et al. 2007).

The light curves in Fig. 10 clearly demonstrates that the AMI rapid-response programme is probing the early-time parameter space of GRBs, between 10^{-3} to 0.1 d post-burst in the rest frame, which has been very poorly sampled until now. The pile up of limits at 10^{-2} days post-burst in the rest frame is likely due to the most common rapid-response time (4.32 min) combined with assuming $z = 2$ for GRBs without a known redshift. The deepest early-time limits (<0.1 d post-burst) are around $\sim 10^{30}$ erg s^{-1} Hz^{-1}. This limit can be improved with longer observing times and the use of more sensitive instruments. Overall, this plot demonstrates a proof of concept for rapid-response telescope triggering on GRBs.

5.4 *Swift* GRB subpopulations

Within the AMI sample there is a sub-sample of *Swift* GRBs that were also detected by *Fermi*-LAT. These include GRB 120729A, GRB 121011A, GRB 130427A, GRB 130702A, GRB 130907A and GRB 150314A (Ackermann et al. 2013). Of these six *Fermi*-LAT GRBs, three were detected with AMI, including GRB 130427A and GRB 130702A, which were the two least radio luminous AMI-detected GRBs (see Fig. 10), and GRB 130907A, which was only detected at early times and also radio faint (as previously mentioned both GRB 130427A and GRB 130907A have the earliest radio afterglow detections with AMI).

Several dark bursts were also observed with AMI, including 11 of the 13 *Swift* GRBs classified as dark bursts by Littlejohns et al. (2015, including GRB 130420A, GRB 130502A, GRB 130514A, GRB 130606A, GRB 130609A, GRB 130907A, GRB 140114A, GRB 140318A, GRB 140518A, GRB 140709A and GRB 140710A), along with GRB 140713A (Castro-Tirado et al. 2014c, note that this list is not necessarily exhaustive). Of the 12 dark bursts observed with AMI, only 3 were detected, including GRB 130907A, GRB 140709A and GRB 140713A, representing 25 per cent of this sub-sample. If we also include the *possible* AMI detection of GRB 140318A and the concatenated detection of GRB 130609A, then the AMI radio detection rate of dark bursts may be as high as ~40–50 per cent. While the detection rates for both the *Fermi*-LAT and dark burst populations are consistent with the implied AMI detection rate of ~44–56 per cent (see Section 5.2), with the *Fermi*-LAT GRBs appearing to favour low-luminosity radio afterglows, these conclusions are based on a small number of events so further GRB monitoring is required to determine if their radio properties differ to the larger *Swift* GRB population.

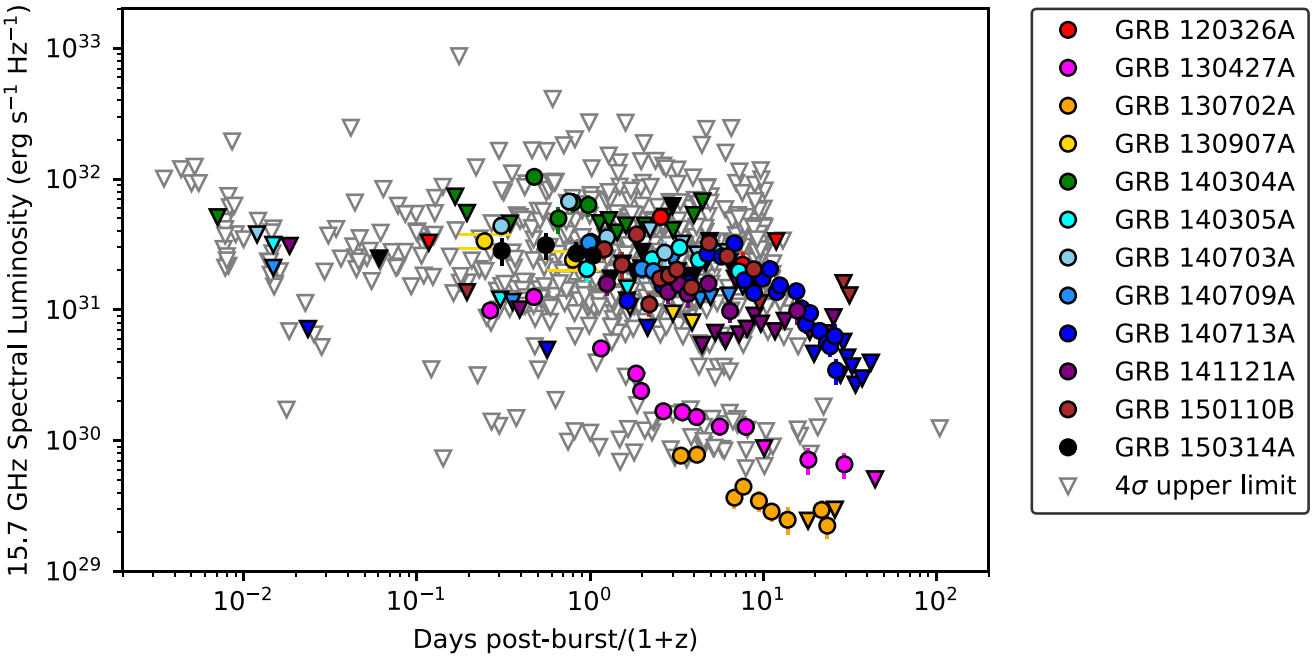

Figure 10. The *k*-corrected spectral luminosity light curve of the 12 *confirmed* AMI-detected GRBs in the rest frame. Each of these 12 GRBs are colour coded with their detections represented as dots and their $4\sigma_s$ upper limits on the non-detections represented by triangles (all errors are $1\sigma_s$). The luminosity $4\sigma_s$ upper limits on all other non-detected GRBs are represented by white triangles. We again assume $z = 2$ for those GRBs without a known redshift. Redshift references: GRB 120326A: Tello et al. (2012), GRB 120404A: Cucchiara & Tanvir (2012), GRB 120422A: Schulze et al. (2012), GRB 120521C: Tanvir et al. (2012b), GRB 120722A: D'Elia et al. (2012), GRB 120724A: Cucchiara et al. (2012), GRB 120729A: Tanvir & Ball (2012), GRB 120802A: Tanvir et al. (2012a), GRB 120811C:Thoene et al. (2012); Fynbo et al. (2012), GRB 120907A: Sanchez-Ramirez et al. (2012), GRB 121128A: Tanvir et al. (2012), GRB 121211A: Perley, Prochaska & Morgan (2012), GRB 130131B: Fynbo et al. (2013), GRB 130418A: de Ugarte Postigo et al. (2013b); Kruehler et al. (2013), GRB 130420A: de Ugarte Postigo et al. (2013a), GRB 130427ALevan et al. (2013); Xu et al. (2013c); Flores et al. (2013), GRB 130505A: Tanvir et al. (2013b), GRB 130511A: Cucchiara & Tanvir (2013), GRB 130514A: Schmidl, Kann & Greiner (2013), GRB 130603B: Foley et al. (2013), Sanchez-Ramirez et al. (2013), Cucchiara, Perley & Cenko (2013), Xu et al. (2013a), GRB130604A: Cenko, Levan & Cucchiara (2013), GRB 130606A: Castro-Tirado et al. (2013b) and Xu et al. (2013e), GRB 130610A: Smette et al. (2013), GRB 130612A: Tanvir et al. (2013c), GRB 130701A: Xu et al. (2013b), GRB 130702A: Singer et al. (2013), GRB 130831A: Cucchiara & Perley (2013), GRB 130907A: de Ugarte Postigo et al. (2013c), GRB 140206A: Malesani et al. (2014b) and D'Elia et al. (2014), GRB 140304A: de Ugarte Postigo et al. (2014d) and Jeong et al. (2014), GRB 140318A: Tanvir et al. (2014a), GRB 140419A: Tanvir et al. (2014b), GRB 140423A: Tanvir et al. (2014c), GRB 140428A: Perley (2014c), GRB 140430A: Kruehler et al. (2014), GRB 140508A: Malesani et al. (2014a) and Wiersema et al. (2014), GRB 140515A: Chornock, Fox & Berger (2014b), GRB 140518A: Chornock et al. (2014c), GRB 140606B: Perley et al. (2014a), GRB 140629A: Moskvitin et al. (2014a) and D'Avanzo et al. (2014), GRB 140703A: Castro-Tirado et al. (2014a), GRB 140710A: Tanvir, Levan & Coulson (2014), GRB 140713A: van der Horst et al. (in preparation), GRB 140801A: de Ugarte Postigo et al. (2014a) and Moskvitin et al. (2014b), GRB 140903A: Cucchiara et al. (2014), GRB 140907A: Castro-Tirado, Gorosabel & Garcia-Rodriguez (2014), GRB 141026A: de Ugarte Postigo et al. (2014c), GRB 141121A: Perley et al. (2014c), GRB 141212A: Chornock, Fong & Fox (2014a), GRB 141220A: de Ugarte Postigo et al. (2014b), GRB 141225A: Gorosabel et al. (2014), GRB 150120A: Chornock & Fong (2015), GRB 150314A: de Ugarte Postigo et al. (2015), GRB 150323A: Perley & Cenko (2015), GRB 150413A: de Ugarte Postigo & Tomasella (2015).

6 SUMMARY AND CONCLUSIONS

Through the AMI GRB follow-up programme, we have produced the first catalogue of radio afterglows that is representative (i.e. not biased by target selection informed by prior knowledge of the event) of the radio properties of *Swift*-detected GRBs down to 0.2 mJy beam^{-1} at 15.7 GHz. This catalogue includes 139 GRBs, 132 of which were detected with *Swift*, and is made up of AMI observations up to >90 d post-burst. This catalogue is also unique in including observations with response times on the order of minutes following the *Swift* GRB trigger, which were performed using ALARRM. AMI is therefore the first radio telescope to target early-time incoherent (afterglow) emission from GRBs at high-radio frequencies (>2.3 GHz) via automatic triggering on *Swift*-BAT detection alerts. As a result, 39 GRBs were observed with AMI using the rapid-response system within <1 h post-burst (mid-time of observation), providing some of the most stringent early-time upper limits of ∼0.2 mJy beam^{-1} at 15.7 GHz.

Using AMI rapid-response and monitoring observations, we have detected radio afterglows from 13 GRBs, 6 of which were discovered as part of this project and thus increasing the rate of GRBs with observed radio afterglows by 50 per cent within an 18-month period. This catalogue also includes a further 6 *possible* AMI-detected GRBs, which cannot be confirmed with our data sets. Based on these results, AMI provides a lower-limit of 15 per cent on the radio detection rate of GRBs down to ∼0.2 mJy beam^{-1}. By including radio GRBs observed but not detected with AMI, as well as the *possible* AMI-detected GRBs, we get a 22–28 per cent detection rate (to an unknown completeness limit), which is more consistent with the ∼30 per cent detection rate obtained by Chandra & Frail (2012). However, if we consider that AMI would have only detected ∼50 per cent of the *Swift* GRBs in the Chandra & Frail (2012) sample, the detection rate could be as high as ∼44–56 per cent down to ∼0.1–0.15 mJy beam^{-1}. We suggest that the early-time (<1 d) observations provided by the AMI rapid-response mode are probing

the fast evolving reverse-shock emission, which we know can have peak fluxes an order of magnitude brighter than the forward-shock (e.g. Anderson et al. 2014e), thus accounting for the ∼20 per cent detection rate increase from the Chandra & Frail (2012) value. Further support comes from six AMI-detected GRBs that peaked within 1 d post-burst in the rest frame. This provides strong evidence that GRB radio afterglow simulations predicting detection rates with the SKA must also take into account contributions from the reverse-shock emission.

The radio afterglows from both GRB 130427A and GRB 130907A were detected during their rapid-response observations, which took place 0.34 and 0.51 d post-burst, respectively, when they had risen above the AMI horizon. Both detections have also resulted in some of the highest recorded minimum Lorentz factors obtained in the radio band (see Table 4 and Anderson et al. 2014e). As they represent the earliest detections obtained with AMI, and also some of the earliest radio detections of long GRBs, it may be prudent to adjust the ALARRM strategy to perform automatic observations between 4 and 16 h post-burst. This slight delay may allow the observations to better coincide with the afterglow emission becoming optically thin at 15.7 GHz.

Luminosity investigations of the AMI data support the conclusion by Chandra & Frail (2012) that GRB radio detection rates are limited by the sensitivity of current radio telescope facilities. However, simulations by Ghirlanda et al. (2013) and Burlon et al. (2015) demonstrate that the forward-shock radio afterglow of *Swift* GRBs will be detectable with SKA1-MID (Band 5), provided that their samples (based on BAT6 GRBs) are representative of the population. Therefore, GRB radio follow-up conducted with the SKA will be able to determine if there is a radio-bright and radio-faint population of GRBs in the *Swift*-detected sample (Hancock et al. 2013).

Since the installation of the new AMI correlator at the end of 2015, the AMI-ALARRM GRB programme has continued, with all new radio afterglow detections and upper limits being reported on the AMI-GRB data base[6] and on the GCN. As the programme continues, AMI will build a larger sample to enable more thorough statistical studies of different *Swift* GRB subpopulations. We will be able to further investigate the radio properties of *Fermi*-LAT-detected GRBs and dark bursts, by establishing their radio detection rates in comparison with the larger *Swift* sample, and confirming whether *Fermi*-LAT GRBs tend to have lower-luminosity radio afterglows.

Rapid-response observing systems represent a new phase in radio transient astronomy. Installing such observing modes on radio telescopes is allowing astronomers to directly test strategies for the SKA facilities, which are baselined to have the same capabilities. Through utilizing the VOEvent network (Staley & Fender 2016), ALARRM is allowing us to probe the unusual parameter space of the early-time (<1 d) radio properties of high-energy transients, and in-turn exploring the scientific payoff of interrupting SKA observing programmes to trigger on these events. This programme has also shown the value of rapid-response systems for radio transient science beyond GRBs, with the early-time detections of the flare star DG CVn (on source within 6 min post-burst; Fender et al. 2015) and the black hole X-ray binary V404 Cyg (on source within 2 h post-burst; Mooley et al. 2015). ALARRM also illustrates the benefits of simultaneous multiwavelength observations (e.g. triggered AMI observations of the flare star DG CVn, which were quasi-simultaneous with X-ray/γ-ray *Swift* observations; Fender et al. 2015) and will hopefully encourage the implementation of other simultaneous multiwavelength experiments (see Middleton et al. 2017).

The ALARRM programme has also prompted the writing of the CHIMENEA and AMISURVEY software packages (Staley & Anderson 2015b), which utilize PYTHON and mature radio reduction software to automate the data reduction and analysis of multi-epoch radio observations. This is the first step to identify transient sources in real time (using software like the TRAP and PYSE), which could be immediately reported to the astronomical community. Overall, the AMI-ALARRM programme is already demonstrating the exciting science that can be probed through early-time detections of high-energy transients, which in turn shows the value in performing real-time transient triggering. We therefore encourage other radio telescopes to equip similar rapid-response capabilities in order to demonstrate that there are no significant barriers to implement such technologies on the SKA facilities.

[6] https://4pisky.org/ami-grb/

ACKNOWLEDGEMENTS

We thank the staff of the Mullard Radio Astronomy Observatory for their invaluable assistance in the operation of the Arcminute Microkelvin Imager. GEA, TDS, RPF and JWB acknowledge the support of the European Research Council Advanced Grant 267697 '4 Pi Sky: Extreme Astrophysics with Revolutionary Radio Telescopes'. AJvdH, AR and RAMJW acknowledge support from the European Research Council via Advanced Investigator Grant no. 247295 'The Amsterdam-ASTRON Radio Transients Facility and Analysis Centre (AARTFAAC)'. KPM's research is supported by the Oxford Centre for Astrophysical Surveys that is funded through the Hintze Family Charitable Foundation. CR acknowledges the support of a Science and Technology Facilities Council studentship.

REFERENCES

Ackermann M. et al., 2013, ApJS, 209, 11
Anderson G. E., Fender R. P., Staley T. D., Rowlinson B. A., 2013, GCN Circ., 15211
Anderson G. E., Fender R. P., Staley T. D., van der Horst A. J., 2014a, GCN Circ., 16603
Anderson G. E., Fender R. P., Staley T. D., van der Horst A. J., Rowlinson A., 2014b, GCN Circ., 16543
Anderson G. E., Fender R. P., Staley T. D., van der Horst A. J., Rowlinson A., 2014c, GCN Circ., 17099
Anderson G. E., Fender R. P., Staley T. D., van der Horst A. J., Rowlinson A., Rumsey C., 2014d, GCN Circ., 16595
Anderson G. E. et al., 2014e, MNRAS, 440, 2059
Anderson G. E., Fender R. P., Staley T. D., Mooley K., van der Horst A. J., Rowlinson A., 2015a, GCN Circ., 17797
Anderson G. E., Fender R. P., Staley T. D., Mooley K., van der Horst A. J., Rowlinson A., 2015b, GCN Circ., 17708
Anderson G. E., Fender R. P., Staley T. D., van der Horst A. J., 2015c, GCN Circ., 17322
Atwood W. B. et al., 2009, ApJ, 697, 1071
Bannister K. W., Murphy T., Gaensler B. M., Reynolds J. E., 2012, ApJ, 757, 38
Barthelmy S. D. et al., 2005, Space Sci. Rev., 120, 143
Barthelmy S. D. et al., 2013, GCN Circ., 14229
Berger E., Cowie L. L., Kulkarni S. R., Frail D. A., Aussel H., Barger A. J., 2003, ApJ, 588, 99
Berger E., Fong W., Chornock R., 2013, ApJ, 774, L23
Blandford R. D., McKee C. F., 1976, Phys. Fluids, 19, 1130
Burlon D., Ghirlanda G., van der Horst A., Murphy T., Wijers R., Gaensler B., Ghisellini G., Prandoni I., 2015, Proc. Sci., The SKA View of Gamma-Ray Bursts. SISSA, Trieste, PoS(AASKA14)052

Burrows D. N. et al., 2000, in Flanagan K. A., Siegmund O. H., eds, Proc. SPIE Conf. Ser. Vol. 4140, X-Ray and Gamma-Ray Instrumentation for Astronomy XI. SPIE, Bellingham, p. 64
Burrows D. N. et al., 2008, preprint (arXiv:0803.1844)
Carbone D., van der Horst A. J., Wijers R. A. M. J., Rowlinson A., 2017, MNRAS, 465, 4106
Castro-Tirado A. J. et al., 2013a, A&A, preprint (arXiv:1312.5631)
Castro-Tirado A. J. et al., 2013b, GCN Circ., 14796
Castro-Tirado A. J., Gorosabel J., Garcia-Rodriguez A., 2014, GCN Circ., 16797
Castro-Tirado A. J. et al., 2014a, GCN Circ., 16505
Castro-Tirado A. J. et al., 2014b, GCN Circ., 16554
Castro-Tirado A. J., Jeong S., Gorosabel J., Reverte D., 2014c, GCN Circ., 16602
Castro-Tirado A. J., Tello J. C., Gorosabel J., Kramer C., Hermelo I., Paubert G., Sievers A., Staguhn J. G., 2014d, GCN Circ., 16974
Cenko S. B., Levan A. J., Cucchiara A., 2013, GCN Circ., 14762
Chandra P., 2013, GCN Circ., 15002
Chandra P., Frail D. A., 2012, ApJ, 746, 156
Cheung T., Vianello G., Zhu S., Racusin J., Connaughton V., Carpenter B., 2013, GCN Circ., 14971
Chornock R., Fong W., 2015, GCN Circ., 17358
Chornock R., Fong W., Fox D. B., 2014a, GCN Circ., 17177
Chornock R., Fox D. B., Berger E., 2014b, GCN Circ., 16269
Chornock R., Fox D. B., Cucchiara A., Perley D. A., Levan A., 2014c, GCN Circ., 16301
Condon J. J., Cotton W. D., Greisen E. W., Yin Q. F., Perley R. A., Taylor G. B., Broderick J. J., 1998, AJ, 115, 1693
Corsi A., 2013, GCN Circ., 15200
Corsi A., 2014a, GCN Circ., 16516
Corsi A., 2014b, GCN Circ., 17019
Corsi A., 2014c, GCN Circ., 17124
Corsi A., Perley D. A., Cenko S. B., 2013, GCN Circ., 14990
Corsi A., Cenko S. B., Cucchiara A., Perley D. A., Horesh A., Frail D. A., 2014, GCN Circ., 17156
Cucchiara A., Perley D., 2013, GCN Circ., 15144
Cucchiara A., Tanvir N. R., 2012, GCN Circ., 13217
Cucchiara A., Tanvir N. R., 2013, GCN Circ., 14621
Cucchiara A., Tanvir N. R., Perley D., Levan A. J., 2012, GCN Circ., 13512
Cucchiara A., Perley D., Cenko S. B., 2013, GCN Circ., 14748
Cucchiara A., Cenko S. B., Perley D. A., Capone J., Toy V., 2014, GCN Circ., 16774
Cucchiara A. et al., 2015, ApJ, 812, 122
Cummings J. R., 2014, GCN Circ., 16765
Cummings J. R. et al., 2014a, GCN Circ., 15934
Cummings J. R. et al., 2014b, GCN Circ., 16354
Cummings J. R., Burrows D. N., Evans P. A., Gehrels N., Kennea J. A., Kuin N. P. M., Page K. L., Palmer D. M., 2014c, GCN Circ., 16763
D'Avanzo P., Malesani D., D'Elia V., Antonelli L. A., Tagliaferri G., Vergani S. D., Fiorenzano A., Mainella G., 2014, GCN Circ., 16493
D'Elia V., Xu D., de Ugarte Postigo A., Malesani D., Fynbo J. P. U., Goldoni P., Tanvir N. R., Kruehler T., 2012, GCN Circ., 13507
D'Elia V., D'Avanzo P., Covino S., Melandri A., Vergani S. D., di Fabrizio L., 2014, GCN Circ., 15802
de Ugarte Postigo A., Tomasella L., 2015, GCN Circ., 17710
de Ugarte Postigo A. et al., 2012, A&A, 538, A44
de Ugarte Postigo A., Tanvir N., Sanchez-Ramirez R., Thoene C. C., Gorosabel J., Fynbo J. P. U., 2013a, GCN Circ., 14437
de Ugarte Postigo A., Thoene C. C., Gorosabel J., Sanchez-Ramirez R., Fynbo J. P. U., Tanvir N., Alvarez Iglesias C. A., 2013b, GCN Circ., 14380
de Ugarte Postigo A., Xu D., Malesani D., Gorosabel J., Jakobsson P., Kajava J., 2013c, GCN Circ., 15187
de Ugarte Postigo A., Gorosabel J., Thoene C. C., Fynbo J. P. U., Xu D., Perez-Valladares D., Gomez-Velarde G., 2014a, GCN Circ., 16657
de Ugarte Postigo A., Thoene C. C., Gorosabel J., Tanvir N., Fynbo J. P. U., Pesev P., Gomez Velarde G., Perez Valladares D., 2014b, GCN Circ., 17198
de Ugarte Postigo A., Thoene C. C., Tanvir N. R., Gorosabel J., Fynbo J., Lombardi G., Reverte-Paya D., Perez D., 2014c, GCN Circ., 16968
de Ugarte Postigo A. et al., 2014d, GCN Circ., 15924
de Ugarte Postigo A. et al., 2015, GCN Circ., 17583
Dessenne C. A.-C. et al., 1996, MNRAS, 281, 977
Dickinson C. et al., 2004, MNRAS, 353, 732
Eichler D., Livio M., Piran T., Schramm D. N., 1989, Nature, 340, 126
Evans P. A. et al., 2014, MNRAS, 444, 250
Fender R. P., Anderson G. E., Osten R., Staley T., Rumsey C., Grainge K., Saunders R. D. E., 2015, MNRAS, 446, L66
Flores H. et al., 2013, GCN Circ., 14491
Foley R. J., Chornock R., Fong W., Berger E., Jha S., 2013, GCN Circ., 14745
Fomalont E. B., 1968, Bull. Astron. Inst. Netherlands, 20, 69
Fong W., 2014, GCN Circ., 16777
Fong W. et al., 2014, ApJ, 780, 118
Fong W., Berger E., Margutti R., Zauderer B. A., 2015, ApJ, 815, 102
Frail D. A., Kulkarni S. R., Nicastro L., Feroci M., Taylor G. B., 1997, Nature, 389, 261
Frail D. A., Waxman E., Kulkarni S. R., 2000, ApJ, 537, 191
Frail D. A. et al., 2000, ApJ, 534, 559
Frail D. A. et al., 2001, ApJ, 562, L55
Frail D. A., Kulkarni S. R., Berger E., Wieringa M. H., 2003, AJ, 125, 2299
Frail D. A., Metzger B. D., Berger E., Kulkarni S. R., Yost S. A., 2004, ApJ, 600, 828
Frail D. A. et al., 2006, ApJ, 646, L99
Franzen T. M. O. et al., 2011, MNRAS, 415, 2699
Fynbo J. P. U., Xu D., Jakobsson P., Armstrong D., Cardenes R., 2012, GCN Circ., 13632
Fynbo J. P. U., Xu D., Malesani D., Kruehler T., Perley D. A., D'Elia V., 2013, GCN Circ., 14286
Gaensler B. M., Hunstead R. W., 2000, PASA, 17, 72
Galama T. J. et al., 1998, ApJ, 500, L101
Galama T. J. et al., 1999, Nature, 398, 394
Gehrels N. et al., 2004, ApJ, 611, 1005
Gehrels N., Ramirez-Ruiz E., Fox D. B., 2009, ARA&A, 47, 567
Ghirlanda G. et al., 2013, MNRAS, 435, 2543
Gorbovskoy E. S. et al., 2016, MNRAS, 455, 3312
Gorosabel J., de Ugarte Postigo A., Thoene C. C., Tanvir N., Fynbo J. P. U., Garcia-Alvarez D., Perez-Romero A., 2014, GCN Circ., 17234
Granot J., Sari R., 2002, ApJ, 568, 820
Granot J., van der Horst A. J., 2014, PASA, 31, e008
Green D. A. et al., 1995, Ap&SS, 231, 281
Guidorzi C., Melandri A., Kopac D., Gomboc A., Mundell C. G., Virgili F., 2014, GCN Circ., 16003
Guilloteau S. et al., 1992, A&A, 262, 624
Hancock P. J., Gaensler B. M., Murphy T., 2013, ApJ, 776, 106
Horesh A., Singer L. P., Cenko S. B., Kasliwal M. M., Perley D., 2014, GCN Circ., 16266
Ivanov K. et al., 2015, GCN Circ., 17689
Jaeger S., 2008, in Argyle R. W., Bunclark P. S., Lewis J. R., eds, ASP Conf. Ser. Vol. 394, Astronomical Data Analysis Software and Systems XVII. Astron. Soc. Pac., San Francisco, p. 623
James D. et al., 2013, GCN Circ., 14713
Jeong S., Sanchez-Ramirez R., Gorosabel J., Castro-Tirado A. J., 2014, GCN Circ., 15936
Jonas J. L., 2009, IEEE Proc., 97, 1522
Kaplan D. L. et al., 2015, ApJ, 814, L25
Kouveliotou C., Meegan C. A., Fishman G. J., Bhat N. P., Briggs M. S., Koshut T. M., Paciesas W. S., Pendleton G. N., 1993, ApJ, 413, L101
Krimm H. A. et al., 2013, ApJS, 209, 14
Krimm H. A. et al., 2014, GCN Circ., 16370
Kruehler T., Xu D., Sanchez-Ramirez R., Malesani D., Fynbo J., Flores H., 2013, GCN Circ., 14390
Kruehler T., Malesani D., de Ugarte Postigo A., Melandri A., Fynbo J. P. U., 2014, GCN Circ., 16194
Kuin N. P. M., Evans P. A., 2015, GCN Circ., 17296
Kulkarni S. R., 2013, The Astronomer's Telegram, 4807

Kulkarni S. R. et al., 1998, Nature, 395, 663
Kulkarni S. R. et al., 1999, ApJ, 522, L97
Laskar T., Zauderer A., Berger E., 2012, GCN Circ., 13181
Laskar T. et al., 2013, ApJ, 776, 119
Laskar T., Zauderer A., Berger E., 2013a, GCN Circ., 14817
Laskar T., Zauderer B. A., Berger E., 2013b, GCN Circ., 14171
Laskar T. et al., 2014, ApJ, 781
Laskar T., Zauderer A., Berger E., 2014a, GCN Circ., 15930
Laskar T., Zauderer A., Berger E., 2014b, GCN Circ., 16283
Lattimer J. M., Schramm D. N., 1976, ApJ, 210, 549
Levan A. J., Tanvir N. R., Wold T., Mason R., 2012, GCN Circ., 13077
Levan A. J., Cenko S. B., Perley D. A., Tanvir N. R., 2013, GCN Circ., 14455
Levan A. J. et al., 2014, ApJ, 781, 13
Liang E., Zhang B., Virgili F., Dai Z. G., 2007, ApJ, 662, 1111
Lien A. et al., 2016, ApJ, 829, 7
Linevsky J. S., Siegel M. H., Grupe D., 2013, GCN Circ., 14928
Littlejohns O. M. et al., 2015, MNRAS, 449, 2919
Lorimer D. R., Bailes M., McLaughlin M. A., Narkevic D. J., Crawford F., 2007, Science, 318, 777
Malesani D., Xu D., D'Avanzo P., Palazzi E., Perna D., 2014a, GCN Circ., 16229
Malesani D. et al., 2014b, GCN Circ., 15800
Margutti R. et al., 2013, ApJ, 778, 18
Mazaeva E., Schmalz S., Tungalag N., Volnova A., Molotov I., Pozanenko A., 2015, GCN Circ., 17305
Meegan C. et al., 2009, ApJ, 702, 791
Melandri A. et al., 2013, GCN Circ., 14223
Mereghetti S., Gotz D., Ferrigno C., Bozzo E., Filippova E., Borkowski J., 2014a, GCN Circ., 16004
Mereghetti S., Gotz D., Ferrigno C., Bozzo E., Filippova E., Borkowski J., 2014b, GCN Circ., 16007
Middleton M. et al., 2017, New Astron. Rev., preprint (arXiv:1709.03520)
Mihalas D., Mihalas B. W., 1984, Foundations of Radiation Hydrodynamics. Oxford University Press, New York, 731 p.
Mooley K., Fender R., Anderson G., Staley T., Kuulkers E., Rumsey C., 2015, Astron. Telegram, 7658
Moskvitin A., Burenin R., Uklein R., Sokolov V., Sanchez-Ramirez R., Gorosabel J., Castro-Tirado A. J., 2014a, GCN Circ., 16489
Moskvitin A., Komarova V., Sokolova T., Castro-Tirado A. J., Gorosabel J., Pandey S. B., Glushkov M., Boronina S., 2014b, GCN Circ., 16663
Narayan R., Paczynski B., Piran T., 1992, ApJ, 395, L83
Nayana A. J., Chandra P., 2014, GCN Circ., 16815
Pagani C., Page K. L., 2014, GCN Circ., 16015
Pagani C., Page K. L., Starling R. L. C., 2014, GCN Circ., 16013
Palaniswamy D., Wayth R. B., Trott C. M., McCallum J. N., Tingay S. J., Reynolds C., 2014, ApJ, 790, 63
Perley D. A., 2013, GCN Circ., 14387
Perley D. A., 2014a, GCN Circ., 15809
Perley D. A., 2014b, GCN Circ., 16122
Perley D. A., 2014c, GCN Circ., 16181
Perley D. A., 2014d, GCN Circ., 16515
Perley D. A., Cenko S. B., 2015, GCN Circ., 17616
Perley D. A., Kasliwal M., 2013, GCN Circ., 14979
Perley D. A., Alatalo K., Horesh A., 2012, GCN Circ., 13175
Perley D. A., Prochaska J. X., Morgan A. N., 2012, GCN Circ., 14059
Perley D. A., Cao Y., Kasliwal M., Kirby E., 2014a, GCN Circ., 16365
Perley D. A. et al., 2014b, ApJ, 781, 37
Perley D. A., Ott C. P., Modjaz M., Fierroz D., 2014c, GCN Circ., 17081
Perley D. A., Hjorth J., Tanvir N. R., Perley R. A., 2017, MNRAS, 465, 970
Perrott Y. C. et al., 2013, MNRAS, 429, 3330
Pietka M., Fender R. P., Keane E. F., 2015, MNRAS, 446, 3687
Piran T., 1999, Phys. Rep., 314, 575
Planck Collaboration XIII, 2016, A&A, 594, A13
Qin Y. et al., 2013, ApJ, 763, 15
Rau A. et al., 2009, PASP, 121, 1334
Rees M. J., Meszaros P., 1992, MNRAS, 258, 41P
Rengelink R. B., Tang Y., de Bruyn A. G., Miley G. K., Bremer M. N., Roettgering H. J. A., Bremer M. A. R., 1997, A&AS, 124, 259
Roming P. W. A. et al., 2005, Space Sci. Rev., 120, 95
Rybicki G. B., Lightman A. P., 1979, Radiative processes in astrophysics. Wiley-Interscience, New York, p. 393
Salvaterra R. et al., 2012, ApJ, 749, 68
Sanchez-Ramirez R., Gorosabel J., de Ugarte Postigo A., Gonzalez Perez J. M., 2012, GCN Circ., 13723
Sanchez-Ramirez R. et al., 2013, GCN Circ., 14747
Sari R., Piran T., 1999, ApJ, 520, 641
Sari R., Piran T., Halpern J. P., 1999, ApJ, 519, L17
Sault R. J., Teuben P. J., Wright M. C. H., 1995, in Shaw R. A., Payne H. E., Hayes J. J. E., eds, ASP Conf. Ser. Vol. 77, Astronomical Data Analysis Software and Systems IV. Astron. Soc. Pac., San Francisco, p. 433
Schmidl S., Kann D. A., Greiner J., 2013, GCN Circ., 14634
Schulze S. et al., 2012, GCN Circ., 13257
Schulze S., Kruehler T., Tanvir N. R., Djupvik A. A., Jakobsson P., 2014, GCN Circ., 15987
Singer L. P. et al., 2013, ApJ, 776, L34
Singer L. P., Cenko S. B., Kasliwal M. M., Fremling C., Dzigan Y., 2014, GCN Circ., 16226
Smette A., Ledoux C., Vreeswijk P., De Cia A., Petitjean P., Fynbo J., Malesani D., Fox A., 2013, GCN Circ., 14848
Soderberg A. M. et al., 2004, Nature, 430, 648
Staley T. D., Anderson G. E., 2015a, Astrophysics Source Code Library, record ascl:1502.017
Staley T. D., Anderson G. E., 2015b, Astron. Comput., 13, 38
Staley T. D., Anderson G. E., 2015c, Astrophysics Source Code Library, record ascl:1504.005
Staley T. D., Fender R., 2016, preprint (arXiv:1606.03735)
Staley T. D. et al., 2013, MNRAS, 428, 3114
Stamatikos M. et al., 2014, GCN Circ., 16584
Stroh M. C. et al., 2014, GCN Circ., 16353
Swinbank J. D. et al., 2015, Astron. Comput., 11, 25
Tanvir N. R., Ball J., 2012, GCN Circ., 13532
Tanvir N. R., Levan A. J., Matulonis T., 2012, GCN Circ., 14009
Tanvir N. R., Fox D., Fynbo J., Trujllo C., 2012a, GCN Circ., 13562
Tanvir N. R. et al., 2012b, GCN Circ., 13348
Tanvir N. R., Levan A. J., Fruchter A. S., Hjorth J., Hounsell R. A., Wiersema K., Tunnicliffe R. L., 2013a, Nature, 500, 547
Tanvir N. R., Levan A. J., Matulonis T., Smith A. B., 2013b, GCN Circ., 14567
Tanvir N. R., Wiersema K., Xu D., Fynbo J. P. U., 2013c, GCN Circ., 14882
Tanvir N. R., Levan A. J., Coulson D., 2014, GCN Circ., 16570
Tanvir N. R., Kruehler T., Schulze S., Karjalainen R., 2014a, GCN Circ., 15988
Tanvir N. R., Levan A. J., Cucchiarra A., Perley D., Cenko S. B., 2014b, GCN Circ., 16125
Tanvir N. R., Levan A. J., Wiersema K., Petric A., Chiboucas K., Miller J., 2014c, GCN Circ., 16150
Tello J. C., Sanchez-Ramirez R., Gorosabel J., Castro-Tirado A. J., Rivero M. A., Gomez-Velarde G., Klotz A., 2012, GCN Circ., 13118
Thoene C. C., de Ugarte Postigo A., Gorosabel J., Sanchez-Ramirez R., Fynbo J. P. U., Gomez Velarde G., 2012, GCN Circ., 13628
Tingay S. J. et al., 2013, PASA, 30, e007
Troja E. et al., 2016, ApJ, 827, 102
Tyurina N. et al., 2015, GCN Circ., 17690
Urata Y. et al., 2014, ApJ, 789, 146
van der Horst A. J., 2007, PhD thesis, Univ. Amsterdam
van der Horst A. J., 2013, GCN Circ., 14987
van der Horst A. J., 2014, GCN Circ., 17104
van der Horst A. J., Kamble A. P., Wijers R. A. M. J., Kouveliotou C., 2009, GCN Circ., 9883
van der Horst A. J. et al., 2014, MNRAS, 444, 3151
van der Horst A. J. et al., 2015, MNRAS, 446, 4116
Veres P., Corsi A., Frail D. A., Cenko S. B., Perley D. A., 2015, ApJ, 810, 31

Vianello G., 2013, GCN Circ., 15197
Vianello G., Kocevski D., Racusin J., Connaughton V., 2013, GCN Circ., 15196
Virgili F. J. et al., 2013, ApJ, 778, 54
Volnova A., Klunko E., Korobtsev I., Eselevich M., Pozanenko A., 2014a, GCN Circ., 16012
Volnova A., Klunko E., Korobtsev I., Eselevich M., Pozanenko A., 2014b, GCN Circ., 16036
Walker M. A., 1998, MNRAS, 294, 307
Wiersema K., Tanvir N., Levan A., Karjalainen R., 2014, GCN Circ., 16231
Winkler C. et al., 2003, A&A, 411, L1
Woosley S. E., 1993, ApJ, 405, 273
Woosley S. E., Bloom J. S., 2006, ARA&A, 44, 507
Xu D. et al., 2013a, GCN Circ., 14757
Xu D. et al., 2013b, GCN Circ., 14956
Xu D., de Ugarte Postigo A., Schulze S., Jessen-Hansen J., Leloudas G., Kruehler T., Fynbo J. P. U., Jakobsson P., 2013c, GCN Circ., 14478
Xu D., Esamdin A., Ma L., Bai C.-H., Feng G.-J., 2013d, GCN Circ., 14927
Xu D. et al., 2013e, GCN Circ., 14816
Xu D. et al., 2015, GCN Circ., 17693
Yu H.-F., Goldstein A., 2014, GCN Circ., 16224
Yurkov V. et al., 2013, GCN Circ., 14929
Zauderer A., Berger E., Laskar T., 2012a, GCN Circ., 13254
Zauderer A., Laskar T., Berger E., 2012b, GCN Circ., 13231
Zauderer B. A., Berger E., Laskar T., 2013, GCN Circ., 14172
Zauderer B. A., Fong W., Berger E., 2014a, GCN Circ., 16593
Zauderer B. A., Laskar T., Berger E., 2014b, GCN Circ., 15931
Zhang B., 2014, ApJ, 780, L21
Zhang S., Jin Z.-P., Wang Y.-Z., Wei D.-M., 2017, ApJ, 835, 73
Zwart J. T. L. et al., 2008, MNRAS, 391, 1545

SUPPORTING INFORMATION

Supplementary data are available at *MNRAS* online.

Table 1. The AMI 15.7 GHz GRB catalogue: GRBs that have been detected or possibly detected with AMI.
Table 2. The AMI 15.7 GHz GRB catalogue: GRBs that were not detected with AMI, have a possible steady source association or a concatenated detection.

Please note: Oxford University Press is not responsible for the content or functionality of any supporting materials supplied by the authors. Any queries (other than missing material) should be directed to the corresponding author for the article.

APPENDIX A: DESCRIPTION OF NEW *POSSIBLE* GRB RADIO AFTERGLOWS DISCOVERED WITH AMI

A1 GRB 120320A

The ALARRM triggered observation of GRB 120320A, which occurred 0.6 d post-burst, detected a $4\sigma_s$ coincident radio source with a flux of 0.38 ± 0.09 mJy beam^{-1}. However, it is also possible this source is an artefact produced by the nearby radio sources NVSS 141009+084149 and NVSS 140957+084108. This single epoch detection was not reported in Staley et al. (2013) likely due to differences in the reduction procedure and our use of an automatic source finder. No source was blindly detected in the follow-up observation that occurred 15.6 d later or in the concatenated image, with $4\sigma_s$ upper limits of 0.36 and 0.25 mJy beam^{-1}, respectively. However, the quality of both epochs are poor, likely resulting from terrestrial interference due to the low declination of 8.7 deg for this GRB. It is therefore not possible to determine if the coincident radio source seen in the first epoch is real. No other radio observations of this event have been reported but there is a single report of a possible detection of a very faint optical counterpart (Levan et al. 2012).

A2 GRB 130625A

A possible radio source was detected within the XRT 90 per cent position error of GRB 130625A in the 2013 July 22 AMI observation, 27 d post-burst, with a flux of 0.59 ± 0.14 mJy beam^{-1} ($4.4\sigma_s$ flux significance). This source was not detected in any of the 5 earlier epochs, nor in the concatenated image. If such a source were steady it should have been detectable with a $>4\sigma_s$ significance in all the AMI observations of this event (with the exception of the 2013 July 3 observation) and at a $>12\sigma_s$ significance in the concatenated image. It is therefore possible that AMI detected the radio counterpart to GRB 130625A over a month post-burst. No optical counterpart was detected for this GRB but the limits are not particularly constraining (Xu et al. 2013d; Linevsky, Siegel & Grupe 2013; Yurkov et al. 2013).

A3 GRB 140209A

AMI possibly detected the radio counterpart to GRB 140209A with a flux of 0.43 ± 0.10 mJy beam^{-1}, corresponding to a $4.2\sigma_s$ significance, during the first AMI observation on 2014 Feb 10 (1.36 d post-burst). The position of this coincident radio source agrees within $2\sigma_p$ of the optical counterpart position (Perley 2014a). All three follow-up AMI observations that occurred 2.5, 4.4 and 9.4 d post-burst did not detect this source even though their rms noise level was improved by at least factor of $\sim$2 when compared to the first observation. All observations were 4 h in duration. The deep concatenated image also did not detect this source but shows a complex region with some evidence for extended emission or uncleanable sidelobes due to the nearby NVSS sources that lie within 2.7–3.6 arcmin from the XRT position. It is therefore difficult to determine if the coincident radio source seen in the 2014 February 10 observation is real. No other radio observations have been reported for this event.

A4 GRB 140318A

The radio counterpart to GRB 140318A was possibly detected with AMI on 2014 March 25 (8 d post-burst), corresponding to a flux of 0.28 ± 0.05 mJy beam^{-1} with a $5.0\sigma_s$ significance. In the concatenated AMI image of GRB 140318A, the possible radio counterpart was also detected with a flux of 0.15 ± 0.03 mJy beam^{-1} and a significance of $4.9\sigma_s$. The position of this radio source agrees with the position of the optical counterpart (Schulze et al. 2014). The light curve in Fig. 3 shows the detection on 2014 March 25 and the $4\sigma_s$ rms noise levels of the other three AMI epochs of GRB 140318A. The concatenated detection, with a similar significance to that of the detection on 2014 March 25, is fainter by a factor of $\sim$2, which is expected for a non-steady source detected in only one of four epochs. The final observation on 2014 March 28 should also have detected the coincident source with a significance of $4.8\sigma_s$ if it were still the same brightest as that measured during the 2014 March 25 epoch. It is therefore quite possible that AMI detected the radio counterpart to GRB 140318A. There have been no other reports of radio observations of this event. However, the faintness of its optical counterpart does suggest that GRB 140318A was a dark burst, where the optical attenuation was likely caused by moderate dust extinction ($0.25 < A_V < 1$; Littlejohns et al. 2015).

A5 GRB 140320C

GRB 140320C was initially detected by *INTEGRAL* (Mereghetti et al. 2014b) and later localized with the XRT (Pagani & Page 2014). AMI detected a $4.1\sigma_s$ significant radio source with a flux of 0.14 ± 0.03 mJy beam^{-1} within the 90 per cent XRT error circle of GRB 140320C on 2014 March 22 (2.1 d post-burst). If this source were steady then it should have been detected at a similar significance during the following AMI observation two days later on 2014 March 24, and at a significance of $7.8\sigma_s$ in the concatenated image. The position of this radio source agrees within $1.04\sigma_p$ of the optical afterglow position (Volnova et al. 2014a,b). No other radio observations were reported for this even. It is therefore possible that AMI detected the radio afterglow of GRB 140320C.

A6 GRB 140607A

AMI detected a $4.8\sigma_s$ significant radio source within $2.7\sigma_p$ of the best BAT position of GRB 140607A (Krimm et al. 2014) on 2014 June 9 (1.75 d post-burst). The other two epochs were far less sensitive so would not have detected this source. However, this radio source was also not detected in the concatenated image, which has comparable sensitivity to the first AMI epoch. It is therefore possible that this radio source could be the afterglow of GRB 140607A.

APPENDIX B: DESCRIPTION OF AMI CONCATENATED DETECTIONS

B1 GRB 130606A

GRB 130606A lies 21.3 arcsec West of NVSS 163736+294742 and has been classed as a dark burst, the optical flux attenuation likely caused by its high redshift of 5.913 (Castro-Tirado et al. 2013b; Xu et al. 2013e; Littlejohns et al. 2015). In the concatenated AMI observation of GRB 130606A, there appears to be two or even three blended sources at the position of this NVSS source and therefore the position of the GRB. Dividing the observations into two separate concatenated images does not show conclusive evidence for variability from any of the blended sources, likely due to the lack of sensitivity. Given the high redshift of GRB 130606A, it is also unlikely that the host galaxy would be resolved by AMI. However, the EVLA-detected radio emission from GRB 130606A at 21.8GHz just 0.6 d post-burst measuring a flux of $\sim$0.1 mJy beam^{-1} (Laskar, Zauderer & Berger 2013a). Further follow-up at mm wavelengths using the Plateau de Bure Interferometer (PdBI; Guilloteau et al. 1992) detected a $\sim$1.5 mJy beam^{-1} source 3.30 d post-burst at 86.7 GHz but had faded below detectability at 7.50 d post-burst (Castro-Tirado et al. 2013a). Given the sensitivity and spatial resolution of the AMI data it is not possible to conclude anything about the nature of the coincident radio source.

B2 GRB 140508A

The optical counterpart to the *Fermi*-GBM detection GRB 140508A (Yu & Goldstein 2014) was quickly detected and identified by iPTF just 0.28 d post-burst (Singer et al. 2014). A late time radio detection was then made 5.2 d post-burst with the VLA at 6.1 and 22 GHz, reporting a 6.1 GHz flux of 0.13 ± 0.01 mJy beam^{-1} (Horesh et al. 2014). AMI did not start observing GRB 140508A until after 8 d post-burst, but there were no detections of this radio counterpart in the individual epochs. However, the concatenated image from the four AMI observations, ranging from 8.93 to 16.79 d post-burst, yielded the blind detection of a $4.9\sigma_s$ source at the UVOT position of GRB 140508A with a flux of 0.12 ± 0.02 mJy beam^{-1}. This flux value is comparable to the VLA 6.1 GHz detection. To investigate if this was radio afterglow of GRB 140508A, we concatenated the first two epochs and the last two epochs separately to see if there was any evidence for variability. However, the two resulting concatenated images were not sensitive enough to detect the coincident radio source seen in the full concatenated image. It is therefore not possible to determine whether the concatenated observation was deep enough to detect the radio counterpart to GRB 140508A or if we instead detected a steady background source.

B3 GRB 140801A

The radio source detected in the concatenated image of GRB 140801A lies 14.6 arcsec SE (within $3\sigma_p$) from the XRT position with a flux of 0.16 ± 0.03 mJy beam^{-1}. This blindly detected source is also within $3\sigma_p$ of NVSS 025617+305552 and WENSS B0253.2+3044, which could mean that all three are the same source. However, the $3\sigma_p$ position error circles may not necessarily overlap between NVSS and WENSS (the position accuracy of WENSS can range from 1.5 to 10 arcsec; Rengelink et al. 1997). Concatenating the early and later epochs into two separate images showed the source flux to be unchanged between these two epochs. It is therefore likely that this radio source is steady and could be a backgrounds source.

B4 GRB 150309A

A $4.8\sigma_s$ radio source lies 1.8 arcmin to the SE of the XRT position at RA (J2000.0) = 18:29:10.92 ($\pm$55.16 arcsec) and Dec. (J2000.0) = +86:24:08.04 ($\pm$4.20 arcsec) in the concatenated image of GRB 150309A. The large error on the RA coordinate of this radio source means it is within a $1.9\sigma_p$ of the XRT position. Combining the early and late epochs into two concatenated images showed that the flux was consistent between the first concatenated epoch and the deep image, and also consistent with the poorer sensitivity of the second epoch concatenation. This radio source is therefore likely steady and not the radio afterglow of GRB 150309A.

APPENDIX C: RADIO-DETECTED GRBS NOT DETECTED WITH AMI

C1 GRB 130603B

The short GRB 130603B was the first claimed case for an associated 'kilonova' (Tanvir et al. 2013a; Berger, Fong & Chornock 2013) and the third radio-detected short GRB (Fong 2014). GRB 130603B was first detected at 4.9 and 6.7 GHz with the VLA, at fluxes of 125.1 ± 14.4 and 118.6 ± 9.1 μJy beam^{-1}, respectively, just 0.37 d post-burst, fading within 2 days and likely representing one of the earliest radio detections of any GRB (Fong 2014). AMI rapidly responded to the *Swift* trigger and was on-target within 5 min post-burst, obtaining a 1 h observation and $4\sigma_s$ upper limit of 0.57 mJy beam^{-1}. Two further observations at 0.13 and 0.95 d post-burst, both 3 h in duration, where then manually scheduled within the next 24 h. Unfortunately, no radio counterpart was detected with AMI within 24 h down to a $4\sigma_s$ upper limit of 0.24 mJy beam^{-1}, but this is consistent with the VLA detections.

C2 GRB 140419A

The only reported radio observation of GRB 140419A is a marginal radio detection of 1.5 mJy beam^{-1} at 93 GHz with CARMA, just 77 min post-burst (Perley 2014b). If real, this is the earliest ever reported radio detection of a GRB. However, no other radio observations have been reported to confirm this. The earliest AMI observation of GRB 140419A, which resulted from the ALARRM trigger, took place 0.38 d post-burst but did not detect a counterpart with a $4\sigma_s$ upper limit of 0.29 mJy beam^{-1}. Another seven follow-up AMI observations were conducted over the following month, but no radio counterpart was detected with the most constraining $4\sigma_s$ upper limit of 0.14 mJy beam^{-1}.

C3 GRB 140515A

GRB 140515A was observed with the VLA at multiple frequencies 0.62 d post-burst and was detected at 21.8 GHz with a flux of $\sim$0.1 mJy beam^{-1} (Laskar, Zauderer & Berger 2014b). AMI was observing GRB 140515A following the ALARRM trigger at 0.26 d post-burst with a further five follow-up observations occurring over the next week. Unfortunately all the AMI observations of this GRB were very poor likely due to increased terrestrial interference at this low observing elevation (Dec. = 15.105°) and perhaps also from artefacts generated by the nearby extended source NVSS 122409+150526. As a result, no radio counterpart to GRB 140515A was detected in any of the AMI observations. However, given that the radio counterpart was reported to be $\sim$0.1 mJy beam^{-1} at 21.8 GHz it would likely have been at the same level or fainter at 15.7 GHz so no sensitive 4 h AMI observation would have been able to detect it.

C4 GRB 140903A

This short GRB was first reported as a possible burst (Cummings et al. 2014c) and later confirmed by Cummings (2014). A radio detection at 6 GHz with the VLA was reported by Fong (2014) just 0.40 d post-burst with a flux $\sim$0.11 mJy beam^{-1}. A later marginal detection ($3.1\sigma_s$) of 0.102 ± 0.033 mJy beam^{-1} at 1.4 GHz was then provided by Nayana & Chandra (2014) using the GMRT. An analysis of JVLA observations (first reported by Fong et al. 2015) at 6.1 and 9.8 GHz was conducted by Troja et al. (2016), with the brightest detection in both bands occurring at 2.51 d post-burst with fluxes 203 ± 13 and 153 ± 10 μJy beam^{-1}, respectively. This event was detectable for up to $\sim$9 d post-burst, the longest lived radio afterglow observed from a short GRB. Analyses performed by both Troja et al. (2016) and Zhang et al. (2017) demonstrate the radio afterglow is consistent with a standard forward-shock model involving a narrow, collimated outflow.

AMI first observed GRB 140903A at 0.93 d post-burst and detected a possible radio counterpart at the XRT position with a flux of 0.72 ± 0.08 mJy beam^{-1}. However, its close proximity to the bright source NVSS 155207+273501, which lies of 1.5arcmin to the SE of GRB 140903A and has a 15.7 GHz flux of 11.67 ± 0.58 mJy beam^{-1}, caused uncleanable structure in the image. We are therefore unable to preclude the possibility that our detection is in fact an artefact, or partly contaminated by an artefact, generated by NVSS 155207+273501 at the XRT position of GRB 140903A. PYSE did not detect any radio sources at the GRB position in the following six AMI observations of this event. However, the significance resulting from a forced fit at the position of the GRB in these observations are extremely high ($>20\sigma_s$). It is possibly that these high significance values could be due to structures and artefacts from NVSS 155207+273501.

C5 GRB 141026A

GRB 141026A was observed with the VLA 6.0 d post-burst, resulting in a clear detection at 6.2 GHz with a flux of 91 ± 7 μJy beam^{-1} (Corsi 2014b). Marginal detections were also obtained with the VLA at 1.1 and 4.3 d post-burst at 21.8 GHz. A non-detection with the IRAM 30m antenna at 150 GHz within a day post-burst was also reported, resulting in a $3\sigma_s$ flux upper limit of 1.2 mJy beam^{-1} (Castro-Tirado et al. 2014d). No radio afterglow was detected in the eight AMI observations of GRB 141026A taken between 3 min to 18.9 d post-burst. The AMI observation taken closest in time to the VLA 6.2 GHz detection took place 6.9 d post-burst, with a $3\sigma_s$ upper limit of 0.31 mJy beam^{-1}. Given the faintness of the afterglow in the VLA observations it is likely that the radio emission was below the sensitivity of AMI for a 4 h observation.

APPENDIX D: COINCIDENT STEADY SOURCES

D1 GRB 130216A

When *Swift*-BAT-detected GRB 130216A, moon constraints prevented follow-up with the XRT and UVOT until nearly 4 d, at which point any possible counterpart had faded below detectability (Melandri et al. 2013). Ground-based optical follow-up did not detect an optical counterpart either. As a result, the best-known position was provided by BAT with an 1arcmin error (Barthelmy et al. 2013). AMI triggered on this *Swift* event and was on-target and observing GRB 130216A for 1 h within 14 min post-burst. A single uncatalogued radio source lying 45 arcsec SW of the BAT position, and therefore within the BAT position error, was detected at RA (J2000.0) = 04:31:34.23 (±0.50 arcsec) and Dec. (J2000.0) = +14:39:36.94 (±0.88 arcsec) (based on the concatenated image) with a flux of 0.87 ± 0.05 mJy beam^{-1}. However, subsequent observations demonstrated that this radio source showed little evidence for variability and was therefore unlikely to be the radio counterpart to GRB 130216A. The force fitted flux reported in Table 2 for the only epoch without a detection taken on 2013-02-17 was conducted at the position of the radio source rather than at the best BAT position.

D2 GRB 140320B

INTEGRAL detected the long GRB 140320B (Mereghetti et al. 2014a) at 09:26:00 UT, which was quickly localized by the *Swift* XRT (Pagani, Page & Starling 2014). AMI obtain five $\sim$4 h observations of GRB 140320A beginning 1.5 d up to 11.5 d post-burst. In each observation, an uncatalogued radio source was detected, lying 11 arcsec SE of the XRT (and the optical Guidorzi et al. 2014) position at RA (J2000.0) = 09:42:15.00 (±1.44 arcsec) and Dec. (J2000.0) = +60:15:56.04 (±1.02 arcsec) (based on the concatenated image) and is therefore well outside the $3\sigma_p$ XRT position error. Given that the offset between the uncatalogued radio source and the GRB XRT position is much larger than the overall position error, as well as the lack of evidence for variability, this source is likely to be a steady field source rather than the radio counterpart to GRB 140320B.

D3 GRB 140606A

GRB 140606A is a short hard burst that was detected by *Swift* (Stroh et al. 2014). Due to lack of counterpart detections, the best position of this GRB comes from the BAT instrument and has a 90 per cent position error of 2.4 arcmin (Cummings et al. 2014b). A blind source search of the concatenated image detected three sources within a $3\sigma_p$ position error. Of these three, the radio source that lies closest to the best BAT position is NVSS 132712+373613, the fluxes of which are reported in Table 2. The source NVSS 132720+373351, which lies within $2\sigma_p$ of the BAT position was also detected. Both NVSS sources were individually detected in the final three epochs. One other uncatalogued radio source was detected in the concatenated image on the very edge of the BAT error circle at RA (J2000.0) = 13:26:58.7 (±9.3 arcsec) and Dec. (J2000) = 37:35:04.3 (±7.4 arcsec) with a flux of 0.21 ± 0.05 mJy beam^{-1} and a significance of 4.1. Both NVSS sources are unlikely to be associated but we cannot rule out that the uncatalogued radio source could be the GRB counterpart.

D4 GRB 141015A

AMI obtained eight observations of GRB 141015A with the majority of observations lasting between 4 and 5 h. On both 2014 October 20 and 2014 October 23, a source was blindly detected at the XRT position of GRB 141015A with a significance of $4.5\sigma_s$ and $4.7\sigma_s$, respectively. However, the $4\sigma_s$ upper limits of the other epochs are consistent with these detections. This source is therefore near the sensitivity limit of AMI for this range of exposure times. As both the detections and the concatenated flux agree within $2\sigma_s$, it is unlikely that this source is transient. Conversely, the most sensitive late time (post-detections) observation of GRB 141015A, taken on 2014 October 25, should have been able to detect the brightest detection seen on 2014 October 20 at a $5\sigma_s$ level. Using these data, it is therefore not possible to confirm if this is the radio afterglow of GRB 141015A or a steady source.

D5 GRB 141020A

During the AMI monitoring of GRB 141020A, the observation taken on 2014 October 24 detected an uncatalogued radio source with a $4.5\sigma_s$ significance just 26 arcsec South of the UVOT position. This same source was detected in the concatenated image with a significance of $4.9\sigma_s$ but with a flux that was a factor of ∼2 lower than what was detected on 2014 October 24. The faintness of this radio source resulted in large positional errors and therefore lies within $4\sigma_p$ of the UVOT position. Given that the detection on 2014 October 24 is very close to the sensitivity of the other five epochs, it is not possible to conclude any evidence for transient activity. While the concatenated flux is a factor of ∼2 fainter than the detection, it is still agrees within $2\sigma_s$. Given the $>3\sigma_p$ position offset between the UVOT position of GRB 141020A and the blindly detection radio source, and the general lack of statistical evidence for variability, it is unlikely that this is the radio counterpart to GRB 141020A.

This paper has been typeset from a TEX/LATEX file prepared by the author.